UNIVERSIDADE DE SÃO PAULO
ESCOLA DE ENGENHARIA DE SÃO CARLOS

Fernando Henrique Tadashi Himeno

Estudo do efeito de um selo no ruído do eslate através de simulação numérica

São Carlos

2018

Fernando Henrique Tadashi Himeno

Estudo do efeito de um selo no ruído do eslate através de simulação numérica

Dissertação apresentada à Escola de Engenharia de São Carlos da Universidade de São Paulo, para obtenção do título de Mestre em Ciências - Programa de Pós-Graduação em Engenharia Mecânica.

Área de concentração: Aeronaves

Orientador: Prof. Dr. Marcello Augusto Faraco de Medeiros

São Carlos

2018

Ficha catalográfica elaborada pela Biblioteca Prof. Dr. Sérgio Rodrigues Fontes da EESC/USP com os dados inseridos pelo(a) autor(a).

Himeno, Fernando Henrique Tadashi
H657e Estudo do efeito de um selo no ruído do eslate através de simulação numérica / Fernando Henrique Tadashi Himeno; orientador Marcello Augusto Faraco de Medeiros. São Carlos, 2018.

Dissertação (Mestrado) - Programa de Pós-Graduação em Engenharia Mecânica e Área de Concentração em Aeronaves -- Escola de Engenharia de São Carlos da Universidade de São Paulo, 2018.

1. Aeroacústica. 2. Eslate. 3. Selo. 4. Lattice-Boltzmann. 5. POD. I. Título.

Eduardo Graziosi Silva - CRB - 8/8907

FOLHA DE JULGAMENTO

Candidato: Engenheiro **FERRNANDO HENRIQUE TADASHI HIMENO**

Título da dissertação: "Estudo do efeito de um selo no ruído do eslate através de simulação numérica".

Data da defesa: 27/04/2018.

Comissão Julgadora: **Resultado:**

Prof. Associado **Marcello Augusto Faraco de Medeiros (Orientador)**
(Escola de Engenharia de São Carlos/EESC)

Prof. Dr. **Elmer Mateus Gennaro**
(Universidade Estadual Paulista "Júlio de Mesquita Filho"/UNESP - São João da Boa Vista")

Prof. Dr. **Sávio Brochini Rodrigues**
(Universidade Federal de São Carlos/UFSCar)

Coordenador do Programa de Pós-Graduação em Engenharia Mecânica:
Prof. Associado **Gherhardt Ribatski**

Presidente da Comissão de Pós-Graduação:
Prof. Associado **Luís Fernando Costa Alberto**

Dedico esse trabalho à todos que me apoiaram durante esses meses, direta e indiretamente. Aos meus amigos e colegas de pesquisa e ao meu orientador, Marcello A. F. de Medeiros. Dedico também aos meus amigos e mestres do grupo de Kendo, em especial ao sensei Yashiro Yamamoto e sensei Harumi Nakahara, que me inspiraram coragem, determinação e paciência ao longo do aprendizado acadêmico e da vida. Em especial, sou grato aos meus amigos mais próximos, Larissa Almeida, Matheus Rocha, Marina Destro e Tainah Castro, que considero parte da minha família. Por fim, dedico a Rodolfo Tonelli pelo companheirismo diário e momentos felizes que passamos nos últimos meses.

ACKNOWLEDGEMENTS

Agradeço à agência de fomento FAPESP, Fundação de Amparo à Pesquisa do Estado de São Paulo, pelo financiamento desse trabalho através do processo $n°2016/02970 - 5$.

Também agradeço o suporte de Daniel Souza Sampaio e Daniel Rodriguez pelos códigos de pós-processamento de sinais e a Felipe Ramos do Amaral pelos dados experimentais dos casos simulados.

Agradeço também a EMBRAER por disponibilizar as licenças do código PowerFLOW utilizado nesse trabalho e também à Escola Politécnica pela disponibilidade dos núcleos do cluster Dumont.

"Você não sabe do que é capaz até precisar fazer."
Marcello A. F de Medeiros

ABSTRACT

HIMENO, F. H. T. **Study of the effect of bulb seal on the slat noise using numerical simulation**. 2018. 92p. Dissertação (Mestrado) - Escola de Engenharia de São Carlos, Universidade de São Paulo, São Carlos, 2018.

The development on Environmental Regulations related to aircraft noise propagated to the vicinity of airports forced the industry to investigate the noise sources and look for alternatives of noise reduction. The current aircraft noise has a large contribution provenient from the airframe, due to the turbofan engine development. One can identify the most relevant sources as the landing gear, flap and slat. Since slat is distributed in almost whole extension it becomes a distributed noise source. The presence of excrescences inside slat cove can changes significantly the recirculating flow and the characteristics of noise generated. We present simulations with PowerFLOW code for MD30P30N high-lift airfoil, with a square section seal attached on slat cove. Results of propagated noise are presented showing the presence of broadband peaks and the differences caused by the seal inclusion. Mean flow shows the presence of an additional recirculation bubble for some positions of the seal. Proper Orthogonal Decomposition was used to identify the coherent structures that could be related to the slat cavity modes and emerges at earlier stages of mixing layer for cases where the seal presence creates a secondary counter-rotating bubble.

Keywords: Aeroacoustics. PowerFLOW. Slat. Cove Seal. Lattice-Boltzmann. POD.

RESUMO

HIMENO, F. H. T. **Estudo do efeito de um selo no ruído do eslate através de simulação numérica**. 2018. 92p. Dissertação (Mestrado) - Escola de Engenharia de São Carlos, Universidade de São Paulo, São Carlos, 2018.

O desenvolvimeto da Legislação Ambiental relacionada ao ruído de aeronaves nas vizinhanças dos aeroportos impulsionou a indústria à investigar as fontes de ruído e buscar alternativas para sua redução. Atualmente, grande parte do ruído de aeronaves é proveniente das superfícies aerodinâmicas e carenagens devido ao desenvolvimento de turbinas com alta razão de derivação. Pode-se identificar como as principais fontes de ruído: o trem de pouso, flapes e eslates. Como o eslate está distribuído em praticamente toda extensão da asa, esse dispositivo representa uma fonte de ruído distribuída. A presença de excrescências dentro da cova do eslate pode alterar significativamente a recirculação do escoamento dentro da cova e as características de ruído do eslate. Esse trabalho apresenta simulações usando o código PowerFLOW para o aerofólio hiper-sustentador MD30P30N, com um selo presente na cova do eslate. Resultados do ruído propagado são apresentados mostrando a presença de picos de banda larga e diferenças causadas pela inclusão do selo. O escoamento médio mostra a presença de uma bolha de recirculação adicional para algumas posições de selo. O método de *Proper Orthogonal Decomposition* também é usado para identificar as estruturas coerentes imersas no escoamento que podem estar relacionadas com os modos de cavidade do eslate e surgem em estágios iniciais para os casos que o selo produz uma bolha secundária contra-rotativa.

Palavras-chave: Aeroacústica. Eslate. Selo. Lattice-Boltzmann. POD.

LIST OF FIGURES

LIST OF ABBREVIATIONS AND ACRONYMS

FW-H	Ffowcs Williams-Hawkings
ICAO	International Civil Aviation Organization
EPNdB	Effective Perceived Noise in Decibels
POD	Proper Orthogonal Decomposition
LST	Linear Stability Theory
TKE	Turbulent Kinect Energy

CONTENTS

1 INTRODUCTION

In order to regulate acceptable noise levels for aircraft, the International Civil Aviation Organization (ICAO) imposes a maximum noise emission for the aircrafts operation in the vicinity of airports in such a way as to impact neighboring communities as little as possible. This maximum noise is calculated by measuring the sound emitted by the aircraft at three points during the take-off and landing maneuvers and then converted to a number that represents the level effectively perceived by the human ear whose scale is called Effective Perceived Noise in Decibels (EPNdB).

The regulation is followed by several airports worldwide and over the years has changed to impose less and less environmental impact. However, some airports have their own noise limits that differ from ICAO, being more stringent. This tendency forces industry to invest in research aimed at improving and developing quieter aircrafts, not only to remain certifiable but also to conquer increasingly demanding markets.

The turbines in landing maneuvers are not much requested, then noise generated by the high-lift surfaces, i.e., slat and flap, become more significant. These devices are responsible for lift increasing at low speed and high angle of attack situations and are basically present in all current large aircrafts. Efforts are made to understand the phenomena that occurs in the near flow around these devices and then try to minimize as much as possible its noise impact maintaining the airfoil lift.

Noise sources related to the high-lift devices are concentrated primarily at the flap edges and near to the slat trailing edge. Although the flap noise is greater in intensity, slat noise is distributed along almost whole span becoming a significant noise source.

The mechanisms of generation of the slat noise are not fully understood. The flow inside slat cove is very complex and its noise depends on various parameters such as geometry, air velocity, angle of attack, deflection angle of the device and gap between the trailing edge and the main element.

All the mentioned parameters were and still are studied for the clean slat geometry. There are still the more complex geometries which include excrescencies such as insulation seals or deicing surfaces that are present in real slats in operation. These geometries are studied because they represent the most real situation observed in the real aircrafts.

The present study focuses in the study of slat noise generation whose geometry has a squared cross section seal attached on its cove. Experimental studies show that a small excrescence could affect drastically the slat acoustic signature. This is shown by the appearance of more intense tonal peaks and frequency shifting compared to the clean geometry case. In order to investigate this problem, a numerical approach is used and the

obtained simulation data is pos-processed by Proper Orthogonal Decomposition (POD). This technique identifies the coherent structures that emmerges along slat shear layer are dependent on the recirculation region behaviour inside slat cove. The bulb seal present in the studied geometry acts precisely in the alteration of recirculating bubbles and, for this reason, it can represent an approach to identify the mechanisms responsible for the slat noise. The Linear Stability Theory (LST) is also applied for investigation of the shear layer most unstables modes and its possible connection to the tonal peaks.

2 SLAT NOISE REVIEW

Main airframe noise sources are identified in Figure 1 (CRIGHTON, 1991; HAYES et al., 1997; FINK; SCHLINKE, 1980). The major contribution comes from the landing gear and high-lift devices such as slat and flap that are designed for lift increasing at low speed and high angle of attack conditions necessary in takeoff and landing maneuvers.

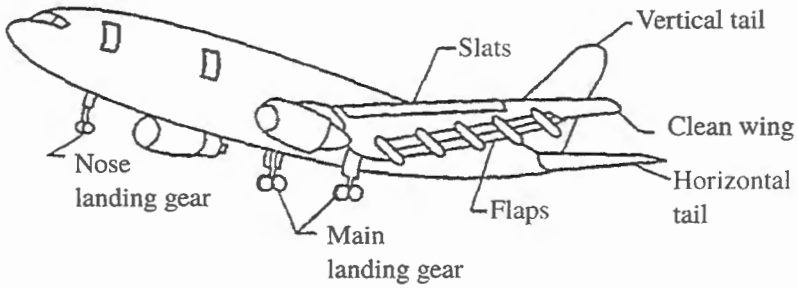

Figure 1: Main airframe noise sources of a aircraft (CRIGHTON, 1991).

Much of the reduction goal until the 1990s was achieved through improvements in turbine design with the inclusion of the bypass technology in turbofans. In fact, with these improvements the intensity of other sources such as aerodynamic surfaces has become much more relevant, especially in the landing condition, where the turbines are at low power. In 1995 the NASA Noise Reduction Program started focusing mainly on noise from airframe and fairings (MACARAEG, 1998; STREETT, 1998; CHOUDHARI; KHORRAMI, 2007; STORMS et al., 1999).

Fink e Schlinke (1980) in a work involving slat, flap and landing gear, showed the slat noise directivity comes from its trailing edge. This is observed by results collapsing into an approximate curve that scales with the fifth power of the velocity, which is also observed by other authors (DOBRZYNSKI et al., 1998).

Dobrzynski et al. (1998) also compares the effect of laminar vortex shedding at the slat cusp with the vortices shedding in cylinders. The noise spectrum peaks disappeared when the boundary layer at the cusp was forced to become turbulent. However, the phenomena was still depended on several other parameters and no characteristic length was found to predict peak frequencies. They also related the high frequency noise to the structures convected by the mixing layer suggesting that they come from quadripoles since the collapse of the curves in this band was better fitted at eighth power speed.

Storms et al. (1999), in a numerical-experimental work varying the angle of attack and slat deflection, suggested that noise mechanism could be related to the vortices shedding at the slat trailing edge. Additionally, they emphasize the complexity of the

mechanism and sudden differences in noise reduction could be some feedback mechanism. This is corroborated by the fact that increasing of flow velocity inside the gap between slat and main element did not increase noise, which would be expected if phenomenona were only dependent of the vortex shedding at the trailing edge.

Roger e Pérennès (2000) suggested the slat cove flow is similar to that observed in open cavities, obtaining good agreement with this theory. The structures generated in the mixing layer reach the cove wall generating an acoustic wave that travels to the cusp and excites the mixing layer generating new structures that close the feedback loop. Evidence of this mechanism is pointed out in the experiments of Takeda et al. (2001).

The slat noise mechanism is still considered complex and dependent of several flow and geometry parameters such as deflection, gap and overlap. Figure 2 outlines a generic noise spectrum that is basically composed of a broadband noise, a high frequency hump and well-defined peaks above the broadband noise.

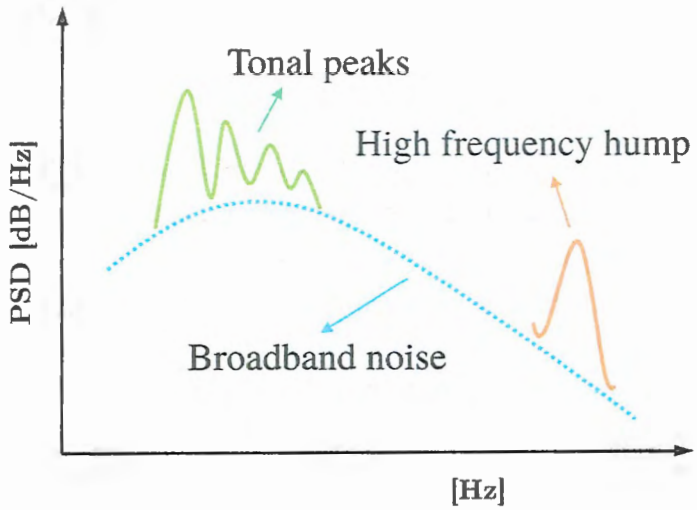

Figure 2: Standart slat noise spectra. (AMARAL, 2015) edited.

The high frequency noise hump is associated with the vortex shedding at trailing edge of the slat because this tonal noise appears only in experiments and simulations where scaled models are used. Such scaled models present a relationship between the trailing edge dimension and airfoil chord which is greater than that found in real wings (KHORRAMI; BERKMAN; CHOUDHARI, 2000). The peaks above the broadband noise are the most controversial components. Dobrzynski e Pott-Polenske (2001) suggested these peaks are associated with vortex shedding at cusp followed by its convection along the mixing layer until they reach the reattachment point near the trailing edge region.

The structures dynamics inside slat cove are presented in Fig. 3. Basically, a laminar flow develops on the slat upper surface that interacts with the cusp. Inside the slat cove a recirculation region is formed interacting with the slat lower surface and mixing layer. The

fluctuations generated in the cusp evolve forming large scale structures that convect along the mixing layer and reach the inner wall at the reattachment point. Then, part of the structures are convected by the recirculation bubble and the remaining is rapidly convected through the gap between slat and the main element (CHOUDHARI; KHORRAMI, 2007).

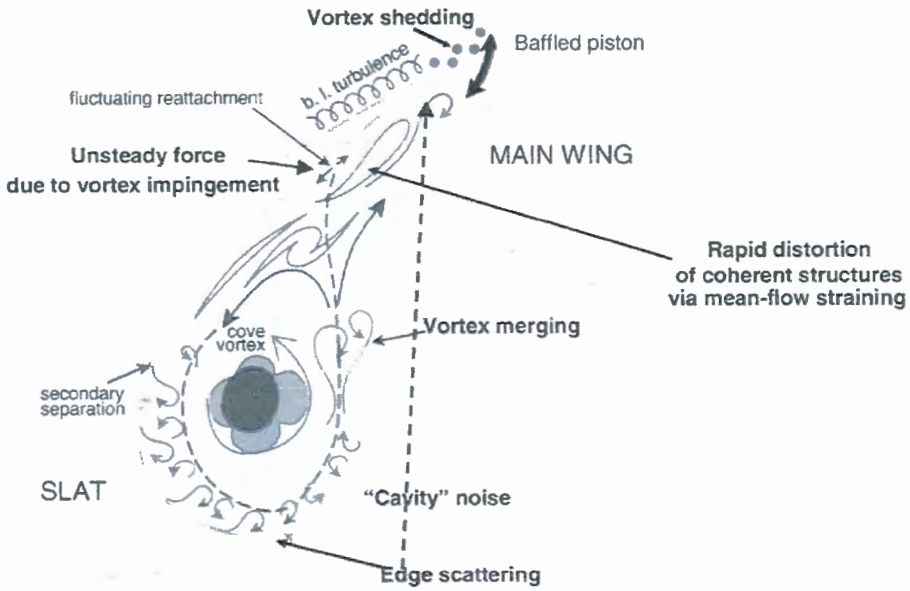

Figure 3: Scheme of the structures dynamics inside slat cove (CHOUDHARI; KHORRAMI, 2007).

Kolb et al. (2007a), recovering the idea of acoustic feedback on cavities, suggested that discrete modes of mixing layer oscillation occur in the slat cove flow. This theory agreed well to the spectra obtained for one of the cases but failed in the trend observed for angle of attack variation, concluding the phenomenona was related to a velocity different than free stream velocity. Subsequently, Manoha et al. (2012) presented a feedback formulation specifically for slat geometry obtaining good agreement for the peaks frequencies.

Khorrami, Singer e Lockard (2002) and Choudhari et al. (2002) in a numerical work, emphasized the importance of the good representation of mixing layer for formation and development of the large scale structures that interact with the recirculation region and do not dissipate. This was done through a URANS code whose turbulence production term was switched off in the cove region.

Choudhari e Khorrami (2007) analyzes the effect of the three-dimensionality of the slat mixing layer. The results suggested the two-dimensionality is observed only in the first stages of the mixing layer, followed by three-dimensionalisation of the vortices until it collides at the reattachment point.

Deck e Laraufie (2013) in a numerical work approximates the velocity profile of the mixture layer by a hyperbolic tangent and applies the Linear Stability Theory (LST) presented by Monkewitz e Huerre (1982a). Their results show that the most unstable

frequencies in the initial stages of the mixing layer agree well with the peaks of velocity fluctuations.

Bres, Pérot e Freed (2009) study the effect of the acoustic dispersion and dissipation between codes based on the Navier-Stokes equations and the Latticce Boltzmann based codes. The results showed that for the same numerical error of acoustic dispersion, the Lattice Boltzmann Method (LBM) used less operations with numbers so the numerical dissipation is lower than that observed in the high order schemes based on the Navier-Stokcs cquations. Thcy also showcd that PowcrFLOW codc shows low numcrical crror for acoustic wavc phasc vclocity comparcd to thc thcorctical valuc.

Even with development in computational resources and numerical algorithms, it is still unfeasible to solve the propagation of acoustic waves from near-field sources to the far-field. Thus, integral techniques that propagate the acoustic information to the far-field overcome this difficulty. The Ffowcs Williams-Hawkings (FW-H) (WILLIAMS; HAWKINGS, 1969) analogy, described by Lockard (2000), is used to predict acoustic signature at various locations using CFD calculation data of non-stationary flow. This analogy is a rearrangement of the Navier-Stokes equations and allows to determine the acoustic signal in far-field if the details of the source region are known. Hence, the Navier-Stokes equations still have to be solved, but only when the non-linear and viscous effects are important (KHORRAMI; LOCKARD, 2010), so that all linear propagation can be determined by this analogy. For three-dimensional flows, the formulation of the FW-H analogy in the time domain was developed by Farassat (1981). This last formulation is implemented in PowerFLOW code.

Most of the studies on slat noise focus on the idealized slat geometry. In real aircrafts, other devices are attached on slat surface such as brackets and seals that can interfere significantly in the noise spectrum. Dobrzynski et al. (1998) had already presented results with a cusp seal and their results showed that the noise spectrum can be drastically affected by minimal changes in geometry. Khorrami e Lockard (2010) analyzed the effect of cusp and bulb seals (Figure 4) concluding the presence of a seal on the cusp reduced the slat noise level and the bulb seal did not seem to considerably change the spectra.

Souza (2012) analyzed the effect of this bulb seal in the slat cove. The parametric study of this seal considered the height and position inside cove wall. The results showed the seal position has a great influence on the flow and on the propagated noise. Far from the reattachment point, the seal causes a substantial change in vortex dynamics. Hence, an increase up to 7 dB/Hz was observed in the slat noise spectrum compared to the baseline configuration. Experiments also corroborate this conclusion with peak intensities even higher than those captured by the simulations (AMARAL et al., 2015).

Souza et al. (2015) using PowerFLOW code and bulb sealed slat geometry, showed by POD analysis that this excrescence increased the coherence of the large scale structures

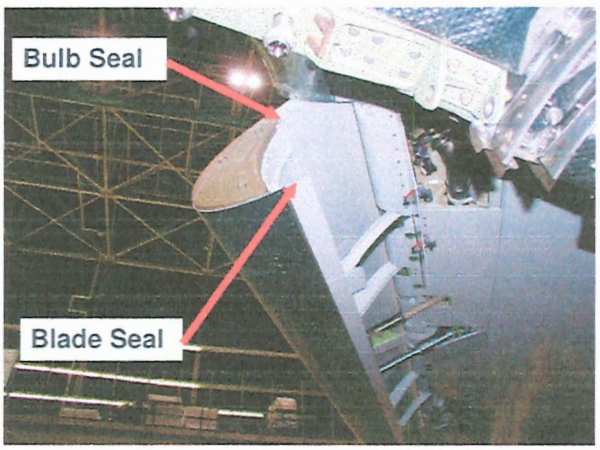

Figure 4: Detail of the Boeing 777 slat showing the cusp and bulb seals (KHORRAMI; LOCKARD, 2010).

in the mixing layer. In addition, the pressure fluctuations outside the cove were correlated with the structures on the wall.

3 METHODOLOGY

3.1 Numerical simulation

3.1.1 Boltzmann equation and modeled collision term

The PowerFLOW code is based on the Lattice Boltzmann Method (LBM) to solve the flow. LBM gained space in CFD (Computational Fluid Dynamics) area compared to the traditional commercial codes because some advantages such as relatively simple code implentation and its simple treatment of complex geometries. Besides, LBM has a high parallelization capacity, allowing a higher processing speed (HE; LUO, 1997). This section presents the LBM, the approximation of collision term and a description of turbulence method implemented in PowerFLOW code.

Macroscopic gas properties such as pressure, velocity and temperature, can be expressed in function of the properties of all the molecules contained in a control volume considering a distribution function, $f(\vec{x}, \vec{\xi}, t)$, which represents the probability of finding a gas molecule at position $\vec{x}$ with a given velocity $\vec{\xi}$ at time t.

The collision effect between the particles is represented by the collision term, Ω, given by the temporal variation of the distribution function:

$$\Omega(\vec{x}, \vec{\xi}, t) = \frac{df(\vec{x}, \vec{\xi}, t)}{dt}. \tag{3.1}$$

Differentiating the distribution function:

$$df = \frac{\partial f}{\partial \vec{x}} d\vec{x} + \frac{\partial f}{\partial \vec{\xi}} d\vec{\xi} + \frac{\partial f}{\partial t} dt \tag{3.2}$$

and dividing by dt, we obtain the collision term, $\Omega(f)$:

$$\Omega(f) = \frac{df}{dt} = \frac{\partial f}{\partial \vec{x}} \cdot \vec{\xi} + \frac{\partial f}{\partial \vec{\xi}} \cdot \vec{a} + \frac{\partial f}{\partial t}. \tag{3.3}$$

If there is no external force, then $\vec{a} = 0$ and this equation becomes:

$$\Omega(f) = \frac{\partial f}{\partial \vec{x}} \cdot \vec{\xi} + \frac{\partial f}{\partial t}, \tag{3.4}$$

that is known as the Boltzmann Equation (BOLTZMANN, 1970) with no external forces. The macroscopic variables are recovered from Boltzmann Equation by the integrals (SOUZA, 2012):

- Mass:

$$\rho = \int f d\vec{\xi}, \tag{3.5}$$

- Momentum:

$$\rho\vec{u} = \int \vec{\xi} f d\vec{\xi}, \tag{3.6}$$

- Energy:

$$\rho\frac{3kT}{2m} = \frac{1}{2}\int (\vec{\xi} - \vec{u})^2 f d\vec{\xi}, \tag{3.7}$$

where k is the Boltzmann constant. The pressure is determined by a Chapmann-Enskog expansion, where the Gas Ideal Law is recovered and then we obtain (CHEN; DOOLEN, 1998; SOUZA, 2012),

- Pressure:

$$p = \rho RT. \tag{3.8}$$

To solve the Boltzmann Equation (Eq. 3.4), we need to know the collision term, Ω. This term, however, is not easily determined since it is a statistical term that represents the particles collisions and requires knowledge of the statistics the particles obey. Then, it is commonly modeled. PowerFLOW approximates Ω as proposed by Bhatnagar, Gross e Krook (1954), so called Ω_{BGK}:

$$\Omega_{BGK}(f) = \frac{1}{\lambda}(f^{eq} - f), \tag{3.9}$$

where λ is called relaxation time and f^{eq} is the steady-state distribution function. PowerFLOW simplifies the term λ as a variable that is not dependent on velocity but only dependent on macrocopics properties such as viscosity and temperature. In Lattice-Boltzmann Method its value is also related to the discretization scheme of the Eq. 3.4. (HE; LUO, 1997; SOUZA, 2012) The f^{eq} term is determined as a Maxwell-Boltzmann distribution function,

$$f^{eq} = \frac{\rho}{(2\pi RT)^{\frac{D}{2}}} e^{-\frac{(\vec{\xi}-\vec{u})^2}{2RT}}, \tag{3.10}$$

where R is the gas constant, T, temperature and $D = 3$ (tridimensional formulation). Expanding the explonential term of Eq. 3.10 and neglecting the fourth order terms, one can obtain

$$f^{eq} = \frac{\rho}{(2\pi RT)^{\frac{D}{2}}} e^{-\frac{\vec{\xi}^2}{2RT}} \left[1 + \frac{\vec{\xi}\cdot\vec{u}}{RT} + \frac{(\vec{\xi}\cdot\vec{u})^2}{2(RT)^2} - \frac{\vec{u}^2}{2RT} + \frac{(\vec{\xi}\cdot\vec{u})^3}{3(RT)^3} - \frac{\vec{\xi}\cdot\vec{u}}{2(RT)^2}\vec{u}^2\right], \tag{3.11}$$

3.1.2 Temporal and spacial discretization

Combining Boltzmann equation and modelled collision term, Eq. 3.4 and 3.9, respectively:

$$\frac{1}{\lambda}(f^{eq} - f) = \frac{\partial f}{\partial \vec{x}} \cdot \vec{\xi} + \frac{\partial f}{\partial t}, \tag{3.12}$$

rearranging,

$$\frac{\partial f}{\partial t} + \frac{\partial f}{\partial \vec{x}} \cdot \vec{\xi} + \frac{1}{\lambda} \cdot f = \frac{1}{\lambda} f^{eq}. \tag{3.13}$$

He e Luo (1997) presents the integration of Eq. 3.13 over a time δt along the characteristic line $\vec{\xi}$,

$$f(\vec{x} + \vec{\xi}\delta t, \vec{\xi}, t + \delta t) = \frac{1}{\lambda} e^{-\frac{\delta t}{\lambda}} \int_0^{\delta t} e^{\frac{t'}{\lambda}} f^{eq}(\vec{x} + \vec{\xi}t', \vec{\xi}, t + t')dt' + e^{-\frac{\delta t}{\lambda}} f(\vec{x}, \vec{\xi}, t), \tag{3.14}$$

subtracting term $f(\vec{x}, \vec{\xi}, t)$ both sides of the Eq. 3.14, we obtain:

$$f(\vec{x} + \vec{\xi}\delta t, \vec{\xi}, t + \delta t) - f(\vec{x}, \vec{\xi}, t) = \frac{1}{\lambda} e^{-\frac{\delta t}{\lambda}} \int_0^{\delta t} e^{\frac{t'}{\lambda}} f^{eq}(\vec{x} + \vec{\xi}t', \vec{\xi}, t + t')dt' + (e^{-\frac{\delta t}{\lambda}} - 1) f(\vec{x}, \vec{\xi}, t), \tag{3.15}$$

Then, with assumption of small δt, local smoothness of f^{eq}, and neglection of second order terms of the right side provided by Taylor expansion of $e^{-\frac{\delta t}{\lambda}}$, Eq. 3.15 becomes: (HE; LUO, 1997)

$$f(\vec{x} + \vec{\xi}\delta t, \vec{\xi}, t + \delta t) - f(\vec{x}, \vec{\xi}, t) = -\frac{1}{\tau}\left[f(\vec{x}, \vec{\xi}, t) - f^{eq}(\vec{x}, \vec{\xi}, t)\right], \tag{3.16}$$

where τ term is the relaxation time non-dimensionalized by δt.

Equation 3.16 is time explicit, given the high parallelization capability of this method. This equation, however, must be solved for each characterisc line given by $\vec{\xi}$. Hence, a discretization of this vector must be provided.

PowerFLOW discretizes the domain in cubic lattices composed of voxels and surfel elements. The voxel is the most basic volume element, being a tridimensional cell. The particles move from a voxel to another at each timestep. The code does not solve this particle movement, but rather particle density distribution function, f. The particles can move in any direction at each voxel but the individual particle density can move only in discrete directions. Velocities and the macroscopic fluid velocity can result in any continuum value of direction and velocity. The surfels are surface elements present in

the intersection of fluid and body. Figure 5 shows a scheme of lattice, voxels and surfels (EXA, 2012). PowerFLOW lattice discretization of characteristic lines is D3Q19 form which represents the tridimensional discretization of 19 vectors as presented in Fig. 6

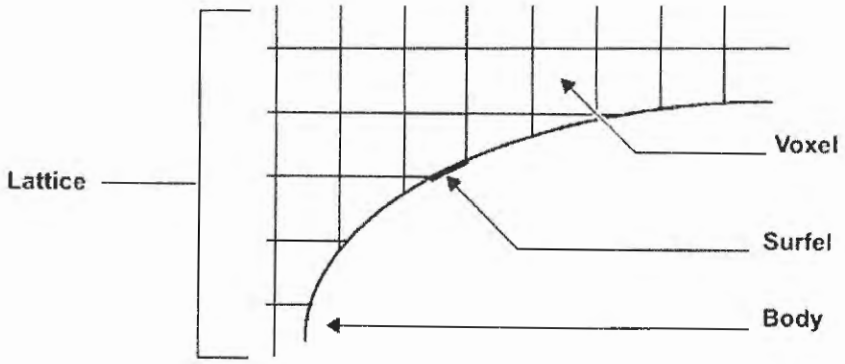

Figure 5: Scheme of Lattice, Voxels and Surfels of PowerFLOW code (EXA, 2012).

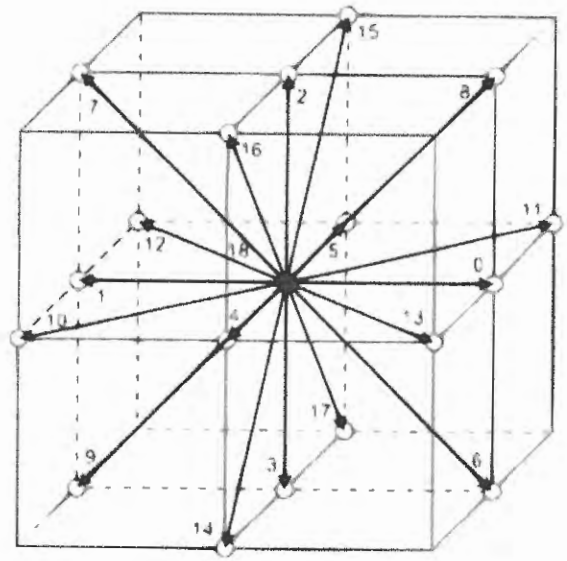

Figure 6: D3Q19 Lattice configuration (SATTI et al., 2008).

Then, with this discretization we have for f_i^{eq}:

$$f_i^{eq} = \rho w_i \left[1 + \frac{\vec{\xi}_i \cdot \vec{u}}{T} + \frac{(\vec{\xi}_i \cdot \vec{u})^2}{2T^2} - \frac{\vec{u}^2}{2T} + \frac{(\vec{\xi}_i \cdot \vec{u})^3}{6T^3} - \frac{\vec{\xi}_i \cdot \vec{u}}{2T^2} \vec{u}^2 \right], \tag{3.17}$$

with weights,

$$w_i = \begin{cases} 1/18, & \text{if} \quad 0 \leq i \geq 5, \\ 1/36, & \text{if} \quad 6 \leq i \geq 17, \\ 1/3, & \text{if} \quad i = 18(rest). \end{cases} \tag{3.18}$$

The discretized Boltzmann Equation becomes:

$$f(\vec{x}+\vec{\xi}_i\delta t,\vec{\xi}_i,t+\delta t)-f(\vec{x},\vec{\xi}_i,t)=-\frac{1}{\tau}\left[f(\vec{x},\vec{\xi}_i,t)-\frac{1}{W_i}f_i^{eq}(\vec{x},\vec{\xi}_i,t)\right], \tag{3.19}$$

where $W_i=(2\pi RT)^{\frac{D}{2}}e^{\frac{\vec{\xi}_i}{2RT}}$ is the quadrature weight that conserves mass and momentum. PowerFLOW also uses an isothermal formulation, then energy equation is not solved and the temperature, T, is considered a constant parameter. Then, the discretized macroscopics properties become

- Mass:

$$\rho(\vec{x},\vec{\xi},t)=\sum_{i=0}^{19}W_i f_i^{eq}(\vec{x},\vec{\xi}_i,t), \tag{3.20}$$

- Momentum:

$$\rho(\vec{x},\vec{\xi},t)\vec{u}(\vec{x},\vec{\xi}.t)=\sum_{i=0}^{18}W_i\vec{\xi}_i f_i^{eq}(\vec{x},\vec{\xi}_i,t). \tag{3.21}$$

The kinematic viscosity is given by

$$\nu=\left(\tau-\frac{\delta t}{2}\right)RT. \tag{3.22}$$

3.1.3 Boundary conditions

In the wall, the calculation is made in the surface center nodes. Figure 7 shows a scheme of lattice discretization D2Q9 just for vizualization of boundary condition on the wall. For no-slip wall we have $f_1=f_3$, $f_5=f_7$ and $f_6=f_8$, considering the collision of particles on the wall to mass and momentum conservation. The free-slip condition becomes $f_1=f_3$, $f_5=f_6$ and $f_7=f_8$.

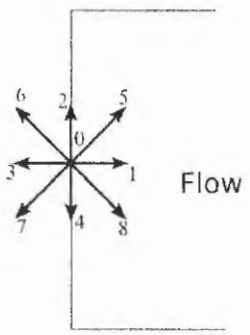

Figure 7: D2Q9 lattice configuration representing discretization on the wall.

Pressure is imposed by the density relation, $p = \rho RT$. Hence, for discretization scheme of Fig. 7 we must solve the distribution functions f_1, f_5 and f_8 that are retrieved by expressions presented in 3.1.2 in a system of equation for density and one equation for each velocity. When velocity is prescribed, an additional relation is needed. Hence, the equilibrium distribution function perpendicular to the wall is assumed, $f_1 - f_1^{eq} = f_3 - f_3^{eq}$ (ZOU; HE, 1997; SOUZA, 2016).

3.1.4 Turbulence model

The small scales structures are modelled by a turbulence model. The two-equation model RNG $k-\epsilon$ (Renormalization-Group $k-\epsilon$) is implemented in PowerFLOW. This model is described by Yakhot e Orszag (1986). The two equations are presented as (SIMõES, 2011)

$$\rho\frac{Dk}{Dt} = \frac{\partial}{\partial x_j}\left[\left(\frac{\rho\nu_0}{\sigma_{k_0}} + \frac{\rho\nu_T}{\sigma_{k_T}}\right)\frac{\partial k}{\partial x_j}\right] + \tau_{ij}S_{ij} - \rho\epsilon, \tag{3.23}$$

$$\rho\frac{D\epsilon}{Dt} = \frac{\partial}{\partial x_j}\left[\left(\frac{\rho\nu_0}{\sigma_{\epsilon_0}} + \frac{\rho\nu_T}{\sigma_{\epsilon_T}}\right)\frac{\partial \epsilon}{\partial x_j}\right] + C_{\epsilon_1}\frac{\epsilon}{k}\tau_{ij}S_{ij} - \left[C_{\epsilon_2} + C_\mu\frac{\tilde{\eta}^3(1-\tilde{\eta}/\tilde{\eta}_0)}{1+\beta\tilde{\eta}^3}\right]\rho\frac{\epsilon^2}{k}, \tag{3.24}$$

where $\nu_T = C_\nu\frac{k^2}{\epsilon}$ and other parameters are constants given by RNG method (YAKHOT; ORSZAG, 1986). Parameter $\tilde{\eta}$ is called swirl and it is related to local deformation and vorticity to increase the turbulent dissipation in regions of high vorticity which decreases the turbulent kinetic energy of $k-\epsilon$ model. This allows the LBM to solve the local large structures. This information of large structures is passed by a temporal relaxation parameter, τ_{ef} which substitutes the τ in the transport equations, (SIMõES, 2011)

$$\tau_{ef} = \tau + C_\mu\frac{k^2/\epsilon}{T\sqrt{1+\tilde{\eta}^2}}. \tag{3.25}$$

3.1.5 Ffowcs Williams-Hawkings analogy

In aeroacoustic problems, we are interested in the propagated noise at positions which generally are in far-field, i.e., not close to the region where the fluctuations of fluid creates the pressure disturbances that generate the noise LIGHTHILL (1952) rearranged the mass conservation and momentum equation presenting a wave equation in which the source term is related to the generated sound. The Ffowcs Williams and Hawkings analogy (FW-H) (WILLIAMS; HAWKINGS, 1969) is based on Lighthill analogy to obtain the wave equation, but for a region around a moving body. FW-H analogy considers a limited source region enclosed in a control surface where the integration is made. PowerFLOW has the FH-W implemented with Farassat 1A formulation (FARASSAT; SUCCI, 1980)

the intersection of fluid and body. Figure 5 shows a scheme of lattice, voxels and surfels (EXA, 2012). PowerFLOW lattice discretization of characteristic lines is D3Q19 form which represents the tridimensional discretization of 19 vectors as presented in Fig. 6

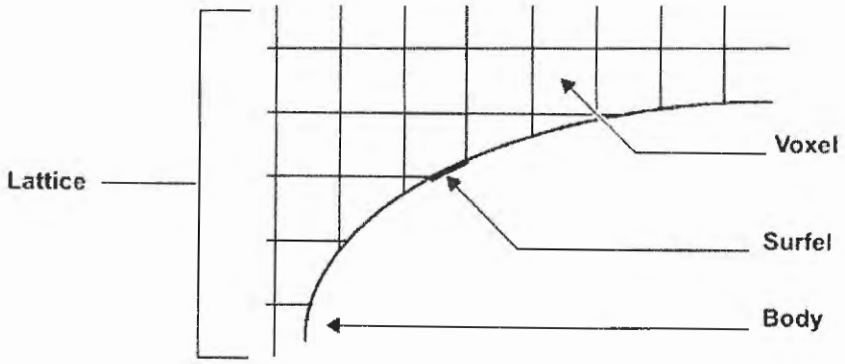

Figure 5: Scheme of Lattice, Voxels and Surfels of PowerFLOW code (EXA, 2012).

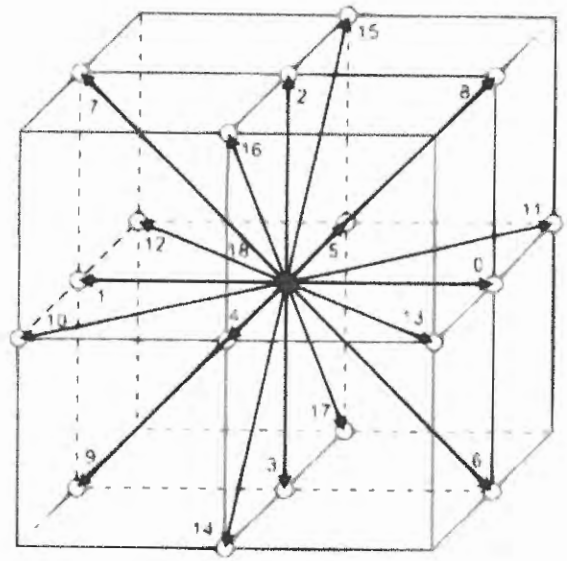

Figure 6: D3Q19 Lattice configuration (SATTI et al., 2008).

Then, with this discretization we have for f_i^{eq}:

$$f_i^{eq} = \rho w_i \left[1 + \frac{\vec{\xi}_i \cdot \vec{u}}{T} + \frac{(\vec{\xi}_i \cdot \vec{u})^2}{2T^2} - \frac{\vec{u}^2}{2T} + \frac{(\vec{\xi}_i \cdot \vec{u})^3}{6T^3} - \frac{\vec{\xi}_i \cdot \vec{u}}{2T^2} \vec{u}^2 \right], \tag{3.17}$$

with weights,

$$w_i = \begin{cases} 1/18, & \text{if} \quad 0 \leq i \geq 5, \\ 1/36, & \text{if} \quad 6 \leq i \geq 17, \\ 1/3, & \text{if} \quad i = 18(rest). \end{cases} \tag{3.18}$$

The discretized Boltzmann Equation becomes:

$$f(\vec{x}+\vec{\xi}_i\delta t,\vec{\xi}_i,t+\delta t)-f(\vec{x},\vec{\xi}_i,t)=-\frac{1}{\tau}\left[f(\vec{x},\vec{\xi}_i,t)-\frac{1}{W_i}f_i^{eq}(\vec{x},\vec{\xi}_i,t)\right], \tag{3.19}$$

where $W_i=(2\pi RT)^{\frac{D}{2}}e^{\frac{\vec{\xi}_i}{2RT}}$ is the quadrature weight that conserves mass and momentum. PowerFLOW also uses an isothermal formulation, then energy equation is not solved and the temperature, T, is considered a constant parameter. Then, the discretized macroscopics properties become

- Mass:

$$\rho(\vec{x},\vec{\xi},t)=\sum_{i=0}^{19}W_i f_i^{eq}(\vec{x},\vec{\xi}_i,t), \tag{3.20}$$

- Momentum:

$$\rho(\vec{x},\vec{\xi},t)\vec{u}(\vec{x},\vec{\xi}.t)=\sum_{i=0}^{18}W_i\vec{\xi}_i f_i^{eq}(\vec{x},\vec{\xi}_i,t). \tag{3.21}$$

The kinematic viscosity is given by

$$\nu=\left(\tau-\frac{\delta t}{2}\right)RT. \tag{3.22}$$

3.1.3 Boundary conditions

In the wall, the calculation is made in the surface center nodes. Figure 7 shows a scheme of lattice discretization D2Q9 just for vizualization of boundary condition on the wall. For no-slip wall we have $f_1=f_3$, $f_5=f_7$ and $f_6=f_8$, considering the collision of particles on the wall to mass and momentum conservation. The free-slip condition becomes $f_1=f_3$, $f_5=f_6$ and $f_7=f_8$.

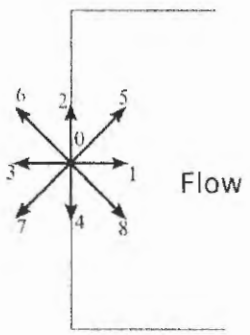

Figure 7: D2Q9 lattice configuration representing discretization on the wall.

which considers a moving permeable surface with quadrupoles inside this surface. Then the equation that describes the problem becomes

$$\frac{\partial^2 \rho'}{\partial t^2} - a_0^2 \frac{\partial^2 \rho'}{\partial x_i^2} = \frac{\partial}{\partial t}\left[Q_n \delta(f)\right] - \frac{\partial}{\partial x_i}\left[L_i \delta(f)\right], \tag{3.26}$$

$$Q_n = \left[\rho_0 v_i + \rho(u_i - v_i)\right] n_i, \tag{3.27}$$

$$L_i = \left[P_{ij} + \rho u_i (u_i - v_i)\right] n_i, \tag{3.28}$$

where vectors $\vec{u}$ and $\vec{v}$ are velocity of fluid and surface, respectively, and $\vec{n}$, the unitary vector normal to surface for each point (SOUZA, 2012). The pressure fluctuation in far-field is given by the sum of thickness and load terms,

$$p'(\vec{x}, t) = p'_T(\vec{x}, t) + p'_L(\vec{x}, t). \tag{3.29}$$

Then, considering the wind tunnel configuration (acoustic source and listener at same velocity) we have the thickness and load terms given by

$$4\pi p'_T(\vec{x}, t) = \int_{f=0} \left[\frac{\frac{\partial Q_i}{\partial \tau} n_i}{R(1 - M_R)^2}\right]_{ret} dS + \int_{f=0} \left[\frac{Q_n a_0 (M_R - M^2)}{R^2 (1 - M_R)^3}\right]_{ret} dS, \tag{3.30}$$

$$\begin{aligned} 4\pi p'_L(\vec{x}, t) = \frac{1}{a_0} \int_{f=0} \left[\frac{\frac{\partial L_i}{\partial \tau} \hat{R}_i}{R(1 - M_R)^2}\right]_{ret} dS + \int_{f=0} \left[\frac{L_i \hat{R}_i - L_i M_i}{R^2 (1 - M_R)^2}\right]_{ret} dS + \\ \int_{f=0} \left[\frac{L_i \hat{R}_i (M_R - M^2)}{R^2 (1 - M_R)^3}\right]_{ret} dS, \end{aligned} \tag{3.31}$$

where the parameters R, M_R and M_0 are constants defined in pre-processing. R is the effective acoustic distance which represents the distance that wave travels which is different from that between the source and listener,

$$R = \frac{-M_0(x_1 - y_1) + \sqrt{(x_1 - y_1)^2 + (1 - M_0^2)[(x_2 - y_2)^2 + (x_3 - y_3)^3]}}{\sqrt{1 - M_0^2}}, \tag{3.32}$$

where M_R, the ratio between the velocity of source/listener on R direction and the sound speed, a_0 (SOUZA, 2012).

3.2 Proper Orthogonal Decomposition (POD)

POD (or Karhunen-Lòeve Decomposition) is a pos-processing tool that identifies the coherent structures inside turbulent flow (BERKOOZ; HOLMES; LUMLEY, 1993). It allows a clearer analysis of the noise generation mechanisms since it represents a filter for the structures related to the determined frequency of interest, in the present case: peaks of the propagated slat noise spectra. This method uses data to generate a set of base functions that optimally represents the energy of the defined inner product, i.e., a finite set of orthogonal modes that better represents the desired flow than any other set of orthogonal basis, highlighting the most energetic structures immersed in the flow (COLONIUS; FREUND, 2002; SOUZA, 2012).

Mathematically, POD finds a finite dimension subspace of a vector space which minimizes the projection error in the subspace itself. Then, the method compacts the information present in large databases such as those produced in experiments and simulations. The main method is presented by (ROWLEY, 2002). The ideia is to find an orthonormal basis $\{\varphi_j \in H | j = 1, ..., n\}$ which the projection of realizations is given by

$$P_S u = \sum_{j=1}^{n} \langle u, \varphi_j \rangle \varphi_j \tag{3.33}$$

where u represents an ensemble of snapshots for each time. Minimizing the average given by $E(||u - P_S u||)$, where $||.||$ represents the norm, it is equivalent to maximizing $E(||P_S u||)$ or $\sum_{j=1}^{n} E(|\langle u, \varphi_j \rangle|^2)$ over the orthonormal functions φ_j which becomes the extremal of the functional

$$J[\varphi] = E(|\langle u, \varphi \rangle|^2) - \lambda(||\varphi||^2 - 1). \tag{3.34}$$

Rewriting the term,

$$|\langle u, \varphi \rangle|^2 = \langle u, \varphi \rangle \langle \varphi, u \rangle = \langle \langle \varphi, u \rangle u, \varphi \rangle = \langle (u \otimes u^*)\varphi, \varphi \rangle. \tag{3.35}$$

Then, using the operator $R = E(u \otimes u^*)$, we have

$$J[\varphi] = \langle R\varphi, \varphi \rangle - \lambda(||\varphi||^2 - 1). \tag{3.36}$$

Since we need the extremal φ, we also need that $\frac{d}{d\delta}\Big|_{\delta=0} J[\varphi + \delta\psi] = 0$. Then, once R is self-adjoint, we obtain

$$\frac{d}{d\delta}\Big|_{\delta=0} J[\varphi + \delta\psi] = \langle R\psi, \varphi \rangle + \langle R\varphi, \psi \rangle - \lambda(\langle \psi, \varphi \rangle + \langle \varphi, \psi \rangle) = 2Re\left[\langle R\varphi - \lambda\varphi, \psi \rangle\right]. \tag{3.37}$$

Therefore, the problem resumes to an eigenvalue problem,

$$R\varphi = \lambda\varphi, \tag{3.38}$$

where φ is an eigenvalue of R. For finite dimension problem composed of m linearly independet vectors, $\vec{u}^k$, and standart inner product, matrix R are simmetric and defined as

$$R_{ij} = E(\vec{u} \otimes \vec{u}^*)_{ij} = \frac{1}{m}\sum_{k=1}^{m} u_i^k u_j^k. \tag{3.39}$$

Since the average energy captured by POD mode, φ, can be expressed by

$$\begin{aligned} E(||P_\varphi u||^2) &= E(\langle P_\varphi u, P_\varphi u\rangle) \\ &= E(\langle\langle u,\varphi\rangle\varphi, \langle u,\varphi\rangle\varphi\rangle) \\ &= E(\langle u,\varphi\rangle\langle\varphi,u\rangle)\langle\varphi,\varphi\rangle \\ &= E(|\langle u,\varphi\rangle|^2). \end{aligned} \tag{3.40}$$

But we see from Eq. 3.38 by taking an inner product with φ, we find

$$\lambda = E(|\langle u,\varphi\rangle|^2). \tag{3.41}$$

Then, the eigenvalue POD, λ_k, represents the energy captured by the eigenvalue φ_k, becoming an important parameter to understand the most relevant structures immersed in turbulent flow. Thus, the higher POD eigenvalue is, more present is the mode in the flow and therefore, the more intense its contribution is on the flow dynamics.

Since we have an ensemble of temporal realizations, u_k, the way to compute the POD is the Method of Snapshots. Then, the average $E(\cdot)$ must be defined as a weighted sum of the snapshots:

$$E(f(u)) = \sum_k \alpha_k f(u_k), \tag{3.42}$$

where α is weight which is greater than zero and satisfies $\sum_j \alpha_j = 1$ and for equal weighting, $\alpha_j = \frac{1}{m}$, where m is the number of realizations. Then, the eigenfunction must be composed of a linear combination of this realization, so it becomes

$$\varphi = \sum_k c_k u_k, \tag{3.43}$$

where c_k can be a complex number. Then, the eigenvalue becomes

$$\begin{aligned} E(u \otimes u^*) \sum_k c_k u_k &= \lambda \sum_k c_k u_k \\ \sum_j \sum_k \alpha_j (u_j \otimes u_j^*) c_k u_k &= \sum_k \lambda c_k u_k \\ \sum_k \left(\sum_j \alpha_k \langle u_j, u_k \rangle c_j \right) u_k &= \sum_k \lambda c_k u_k \\ \sum_j \alpha_k \langle u_j, u_k \rangle c_j &= \lambda c_k, \end{aligned} \tag{3.44}$$

which is the eigenvalue problem to solve with matrix R, $m \times m$ dimension (m is the number of realizations) with $R_{ij} = \alpha_k \langle u_j, u_k \rangle$.

The present study uses the spectral formulation of POD as proposed by Sirovich (1987). The basic difference between the standart Snapshot Method is that the vectors used in calculations are the Fourier transformed of signals. Thus, time domain is divided into blocks with some overlap and Fourier transformed for POD calculation. This procedure creates a matrix $\tilde{R}$, given by the cross-correlation matrix composed of inner products among the different snapshots (SOUZA et al., 2015). Then, the eigenvalue problem becomes

$$\tilde{R}\beta_k = \lambda_k \beta_k, \tag{3.45}$$

where the POD functions are recovered by a sum of the vectors $\vec{q}_i$ weighted by eigenvectors:

$$\phi_k = \sum_l \beta_l^k \vec{q}_l. \tag{3.46}$$

The appropriate inner product is very important depending on what we desire to investigate inside the flow. A generic inner product can be represented by equation

$$\langle \vec{q}_i, \vec{q}_i \rangle = \int_\Omega (u_i \sigma_u(\vec{x}) u_j^* + v_i \sigma_v(\vec{x}) v_j^* + w_i \sigma_w(\vec{x}) w_j^* + p_i \sigma_p(\vec{x}) p_j^*) dV, \tag{3.47}$$

where u, v and w are velocity components and p, pressure. The weighting vector is given by $\vec{\sigma}(\vec{x}) = [\sigma_u, \sigma_v, \sigma_w, \sigma_p]$. The turbulent kinetic energy norm has $\vec{\sigma}(\vec{x}) = [1, 1, 1, 0]$ for $\vec{x}$ in the nearfield region and zero in the farfield, then we have

$$P_{TKE} = \int_\Omega (u_i u_j^* + v_i v_j^* + w_i w_j^*) dV, \tag{3.48}$$

for the acoustic intensity norm (SOUZA, 2016), $\vec{\sigma}(\vec{x}) = [0, 0, 0, 1]$ for $\vec{x}$ in farfield and zero at any other point. Then, it becomes

$$P_{Pff} = \int_{\Omega} (p_i p_j^*) dV. \tag{3.49}$$

Considering the correlation of pressure outside the slat cove we expect to obtain the dominant fluctuations that are related to the propagated noise. Some scheme of the points in farfield inner produc, P_{Pff}, that is considered far enough from the nearfield fluctuations is presented in Fig. 8.

Figure 8: Points outside the cove used for farfield inner product, P_{Pff}.

3.3 Linear Stability Theory (LST)

The theory of small perturbations considers a stream function given by

$$\Psi(x, y, t) = \phi(y)e^{i\alpha(x-ct)}, \tag{3.50}$$

where α is the wave number, c, phase velocity which is related to temporal frequency, ω by relation $c = \omega/\alpha$. The eigenfunction is derived by relating the ϕ function with the velocity profile perpendicular to the streamwise direction for a given point at the mixing layer. Substituting in the Navier-Stokes equations and rearranging the terms, one can obtain the Rayleigh equation,

$$[U(y;\lambda) - c](\phi'' - \alpha^2\phi) - U^{*''}(y;\lambda)\phi = 0. \tag{3.51}$$

The velocity profile, U, is approximated to a tanh profile as done by Monkewitz e Huerre (1982b), Huerre e Monkewitz (1990),

$$U^*(y^*) = (\Delta U/2)tanh(2y^*/\delta_\omega) + \overline{U}, \tag{3.52}$$

where y^* is the coordinate of velocity profile, ΔU, the difference between maximum and minimum velocity of this profile and is $\overline{U}$ its mean value, $\delta_\omega = \Delta U^*/(\frac{dU}{dy^*})_{max}$, the vorticity thickness. Numerical results are presented by (MONKEWITZ; HUERRE, 1982b) and the Fig. 9 shows the amplification rate and the most unstable frequencies, i.e., the frequency at which the amplification rate is maximum, of the mixture layer as a function of the parameter λ.

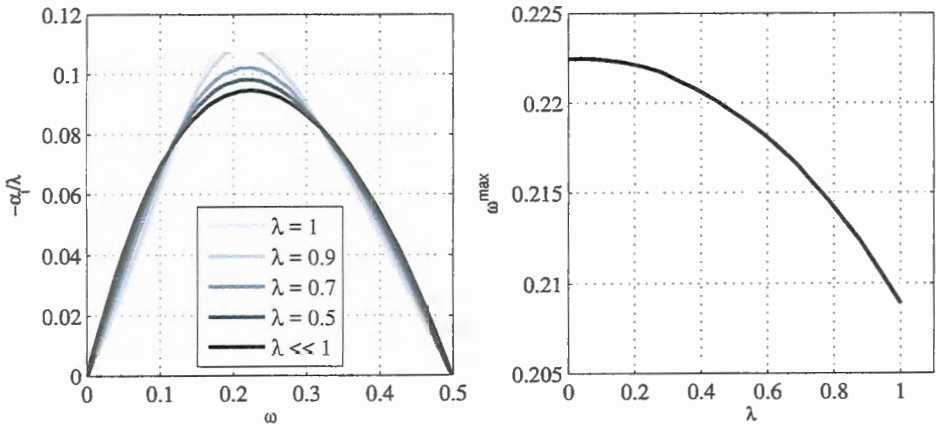

Figure 9: Amplification rate versus frequencies (MONKEWITZ; HUERRE, 1982b) and behaviour of the most unstable frequency in function of $\lambda = \frac{\Delta U}{2\overline{U}}$ parameter. Non-dimensionalization made by $\overline{U}$ and $\frac{\delta_\omega}{4}$.

To solve the Rayleigh Equation, 3.51, the procedure used in this work was the use of a tutorial code provided by Juniper, Hanifi e Theofilis (2014), which solves the temporal instability case. Then, this code was modified to solve the spatial instability that is the interest of this work, i.e., the behaviour of the most unstable modes present in the mixing layer of slat cove.

Hence, Eq. 3.51 can be rearranged to an eigenvalue problem,

$$\boldsymbol{A}\phi = \omega \boldsymbol{B}\phi, \tag{3.53}$$

with matrix $\boldsymbol{A}$ and $\boldsymbol{B}$ given by

$$\begin{aligned} \boldsymbol{A} &= \alpha\overline{U}\left(D^2 - \alpha^2\right) \\ \boldsymbol{B} &= D^2 - \alpha^2, \end{aligned} \tag{3.54}$$

where D represents a derivative operator. Originally the code solved the temporal problem, then, α was a fixed value and the eigenvalue problem solved for ω. If the imaginary part of ω is non-zero, the disturbances grow or decay in time. But for spatial instability, we need to find values of α that give a real temporal frequency. The code modification was made by using *fsolve* tool from Matlab to find, with a range of α values as input, ω whose imaginary part was zero.

Once, obtained the amplification rate ($Im(\alpha) = \alpha_i$) of the perturbations, the spatial amplification, A, is calculated fixing the temporal frequency, ω, and integrating along the mixing layer with a given initial amplitude, A_0, at position L_0,

$$A = A_0 e^{\int_{L_0}^{L} \alpha_i dx}. \tag{3.55}$$

The input parameter for this method is the velocity profile perpendicular to the mixing layer approximated to a hyperbolic tangent profile. Some important parameter given by this fit is the δ_ω, the vorticity thickness, that gives some ideia of thickness development of the mixing layer.

4 PRELIMINARY NUMERICAL STUDIES

4.1 Review of experimental data used for numerical validation

This section presents some review of the simulated high-lift airfoil model and the parameters of experimental data which were used to validate the simulations. The simulated airfoil was MD30P30N (Fig. 10) that is a high-lift airfoil vastly studied in aeroacoustics (KHORRAMI; SINGER; LOCKARD, 2002; JENKINS; KHORRAMI; CHOUDHARI, 2004; SOUZA, 2012; SOUZA et al., 2015). The geometric parameters of the model are presented in Tab. 3. All the edges were considered sharp except the slat trailing edge where the thickness was 0.092% of c_{stowed}.

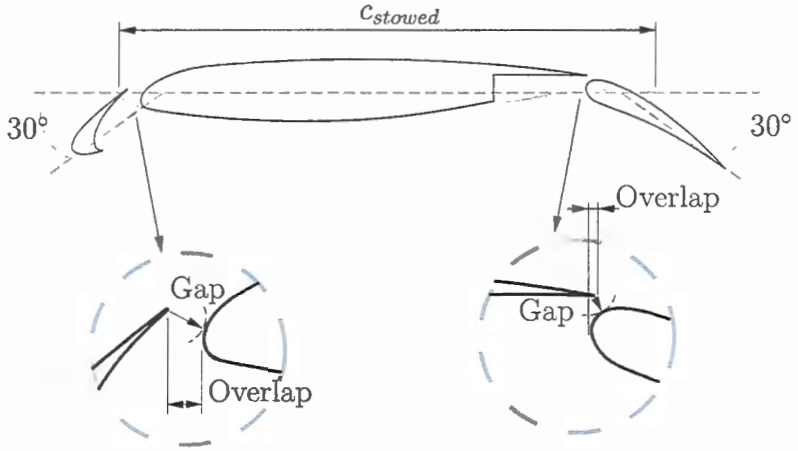

Figure 10: MD30P30N high-lift airfoil and main geometry parameters.

Table 1: Geometrical parameters of MD30P30N airfoil in percentage of c_{stowed}.

	Chord	Deflection	Gap	Overlap
Slat	15 %	30 [°]	2.95 %	−2.50 %
Flap	30 %	30 [°]	1.27 %	0.25 %

The experiments were performed in the LAE wind tunnel of the School of Engineering of São Carlos-USP by Amaral (2015). The model was manufactured in SAE7075 aluminum alloy with pressure tappings in the middle span along a chordwise line and distributed along the span on the suction side, near the main element leading and trailing edges. The slat and flap also had a portion in the middle span that was prototyped to install the static pressure tapping, 143 in chordwise direction and 40 in spanwise. The tunnel has a test section of 1.30 m high, 1.67 m wide, and 3.00 m long. An axial fan with 8 blades with 115 HP of power generating flow speed between 10 and 45 m/s. The contraction ratio is 1 : 8 and the turbulence level is around 0.25%. Boundary layer suction

was applied on the walls around the model at main element suction side and slat trailing edge.

The antena was compound of 62 1/4-inch 40BD G.R.A.S. Sound & Vibration microphones disposed in an optimized Archimedean single-arm spiral. The pos-processing was done by a conventional beamforming technique and DAMAS, assuming the wave propagation under a free field condition emanating from a distribution of uncorrelated monopole point sources. Figure 11 presents an image of the model and antena of the experiments (AMARAL, 2015).

Figure 11: MD30P30N airfoil at wind tunnel (AMARAL, 2015).

The acoustic data was composed of the microphone time series which were divided in blocks with 50% of overlap, Hanning windowed to generate the cross-spectral matrix. Then, the Fourier transform was applied and the outer product between pairs of microphones is calculated. The microphones sampling rate was $51,200\ Hz$ and spectra results were presented in different frequency resolutions for each block size depending on the frequency band (Tab. 2) (AMARAL, 2015).

Freq. band [kHz]	Resolution [Hz]	N blocks
0.50 – 1.60	25	1947
1.65 – 3.20	50	3895
3.30 – 6.40	100	7791
6.60 – 12.80	200	15584
13.20 – 18.00	400	31170

Table 2: Frequency resolution for each frequncy band employed for Power Spectral Density.

4.2 Tests of numerical parameter independency

This section shows some numerical parameters and also the independency tests of the simulation that includes the seal as excrescence. For this analysis the results of the baseline case and the sealed case 0.41 h3w3 are presented, where the angle of attack of both cases is 3°. The nomenclature of sealed case indicates the seal position, $d = 0.41$ non-dimensionalized by c_{slat}, seal height and width of $h = w = 3\ mm$. For visualization, Fig. 12 displays the slat geometry of this sealed case.

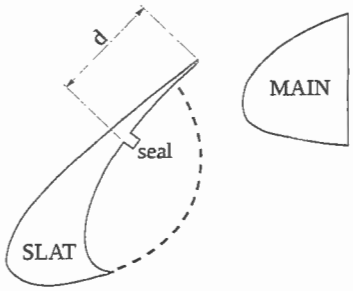

Figure 12: Seal 0.41 h3w3 slat geometry showing the measurement of seal position, d.

Earlier studies on baseline configuration (SIMõES; SOUZA; MEDEIROS, 2011; SOUZA; RODRIGUEZ; MEDEIROS, 2013) but with higher angle of attack (4°) were also used as input parameters for the present simulations of the sealed configurations. The horizontal velocity component of 34 m/s was imposed at the inlet for the reproduction of the experimental setup. The timestep was $3.3287 \times 10^{-7}\ s$. The turbulence intensity defined as the ratio between turbulence velocity fluctuation and inlet velocity was applied and corresponded to a value of 0.0009. Pressure was fixed at $10^5\ Pa$ at the outflow. The vertical extension of the computational domain was fixed to the corresponding wind-tunnel dimension, i.e., 1.7 m height, and the tunnel walls were modelled as free-slip walls. An anechoic layer was also used for damping the acoustic waves that approached the computational domain in horizontal boundaries.

The domain horizontal length used for the sealed cases was the same of previous baseline works of Simões, Souza e Medeiros (2011) Souza, Rodriguez e Medeiros (2013), since the lift was not affected by the seal compared to experimental data. The computational span length was 10% of the model chord, then simulated span was 51.2 mm with a periodicity condition employed in this direction.

Domain refinement level scheme is presented in Fig 13. Levels 7 and 1 have the finest and coarsest cells, respectively, which correspond to 0.2 mm and 12.8 mm edges. The total number of cells was approximately 87×10^6, of which 30% corresponded to the finest ones (level 7), where baseline case was taken as reference. Figure 14 gives some ideia of the mesh refinement level by the plot of center cells around the slat device for seal 0.41

h3w3 and a zoom near the seal neighborhood showing the number of cells compared to seal edge.

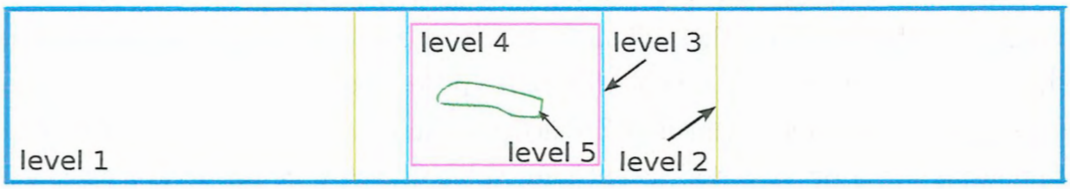

(a) Domain and levels of refinement

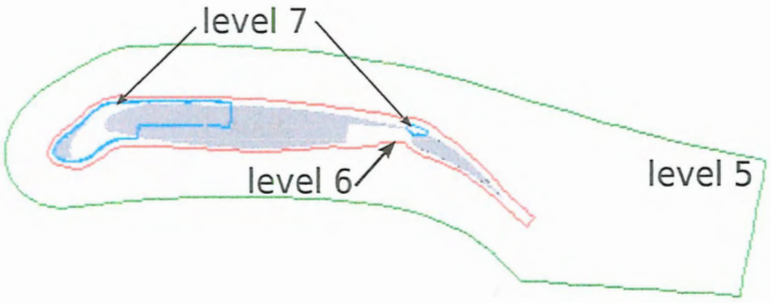

(b) Detail close to airfoil

Figure 13: Domain and levels of mesh refinement (SOUZA, 2016).

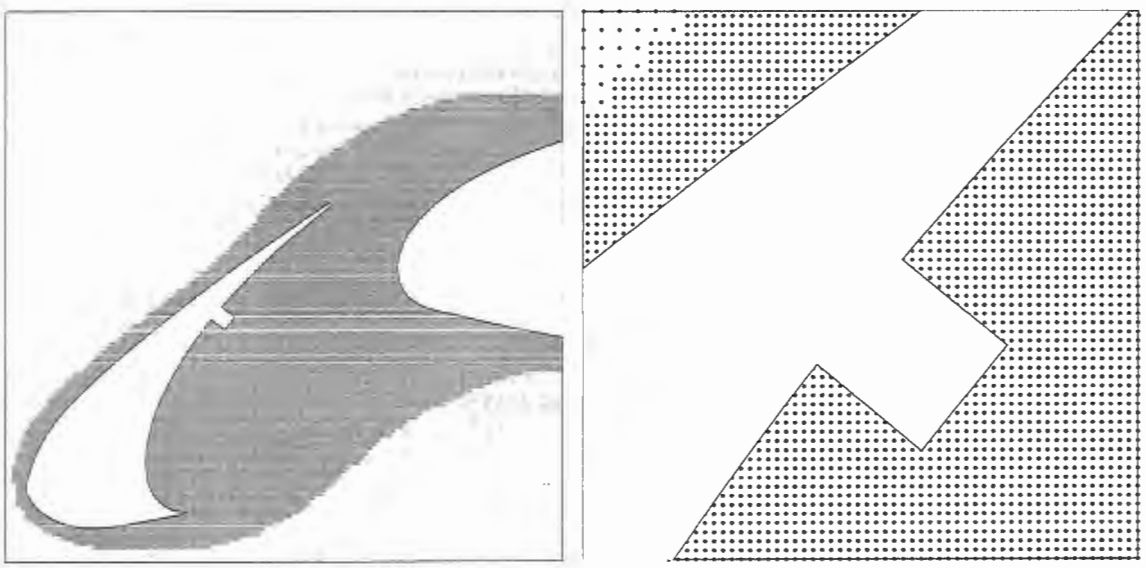

(a) Mesh around the slat device

(b) Detail close to seal

Figure 14: Cells center for seal 0.41 h3w3 showing the refinement level close to the region of interest and zoom around the seal region.

Figure 15 displays a comparison between the pressure distribution obtained numerically and experimentally for baseline and seal 0.41 h3w3 cases. A good agreement was achieved and the numerical results confirmed the seal inclusion did not affect the airfoil aerodynamic performance in comparison to the baseline geometry.

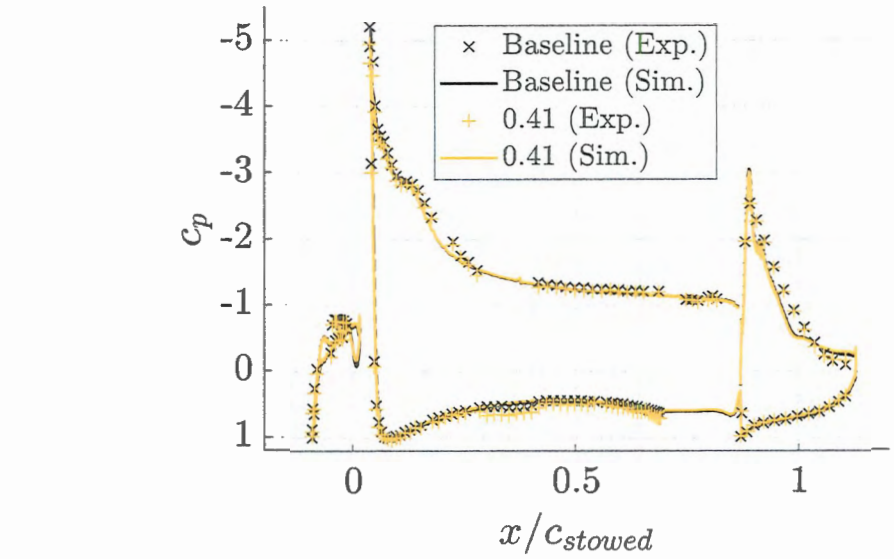

(a) Model chordwise c_p

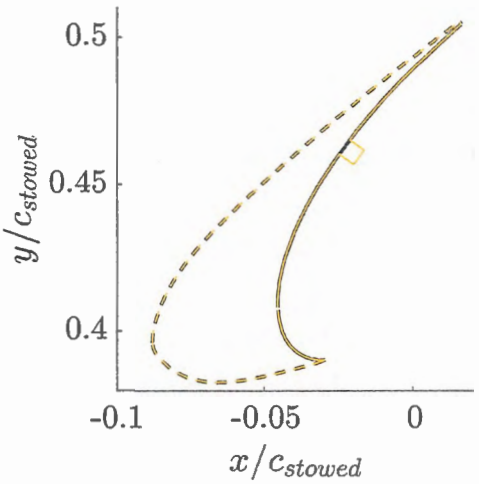

(b) Slat upper and lower surfaces

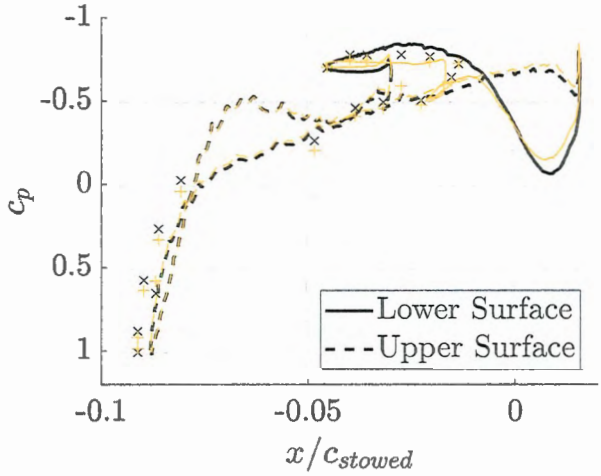

(c) Slat chordwise c_p

Figure 15: Comparison between numerical and experimental pressure coefficients, c_p, over the airfoil.

Figure 16 shows the acoustic spectra numerically and experimentally obtained for seal 0.41 h3w3 case. The narrowband peaks frequencies were well captured but their magnitude were underestimated by the simulation. The mesh refinement may not have been enough to capture the effect of such a small seal, therefore, another simulation was performed with a 0.14 mm, the finest cell edge. The numerical results were independent of the grid, Fig 16, and the disagreement with the experiment could not be overcome by a further mesh refinement. Moreover, the mesh refinement was not sufficient for properly resolving the vortex shedding at the slat trailing edge, which is associated with the high frequency hump of the slat noise spectrum. Since this mechanism is well understood and not relevant in full-scale high-lift configurations (DOBRZYNSKI, 2010) and, as shown

by the current experimental results, not affected by the seal, no action was undertaken regarding this limitation.

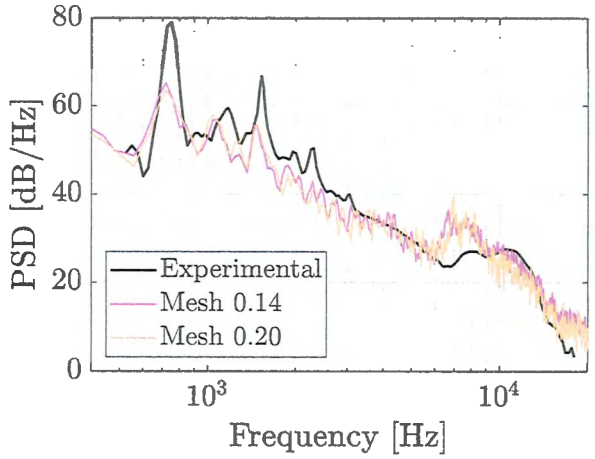

Figure 16: Results of far-field noise spectra mesh refinement tests for case seal 0.41 h3w3.

The coherence of pressure disturbances in spanwise direction at reattachment point was analyzed similar to Lockard e Choudhari (2009), Pagani Jr, Souza e Medeiros (2016). As a function of span position and frequency, the coherence ($\gamma^2(\Delta z, f)$) was calculated as presented in Eq. 4.1, where G_{z_1,z_2} is the cross-spectral power density function of two signals measured at z_1 and z_2, distant Δz between each other. Figure 17 shows a contour plot of the coherence level considering 128 equally spaced points in the center half span of the baseline and sealed configuration 0.41 h3w3. Results show that sealed case presents a higher coherence level mainly for narrowband peaks, however, both cases show that coherence decreases in span.

$$\gamma^2(\Delta z, f) = \frac{G^2_{z_1,z_2}(\Delta z, f)}{|G_{z_1,z_1}(f)||G_{z_2,z_2}(f)|}. \tag{4.1}$$

Following Lockard e Choudhari (2009), Pagani Jr, Souza e Medeiros (2016), the coherence was fitted in a gaussian function (Eq. 4.2) to avoid its dependency of span position. The contour plots in Fig. 18b display the result of this fitting. Compared to Fig. 17, this fitting overestimates the coherence level of initial points in span but maintains the peaks information observed previously. This fitting allows the analysis of coherence length (L_c) that is a parameter of the gaussian fitting only dependent of frequency. Figure 20a shows the result of L_c normalized by slat chord for both baseline and seal 0.41 h3w3. The comparison between the coherence and its gaussian approximation is presented in Fig. 20b for the most proeminent peak of coherence length for baseline and sealed case 0.41 h3w3. The gaussian fitting and L_c peaks found are very similar to that observed in early studies for baseline geometry (PAGANI JR; SOUZA; MEDEIROS, 2016). Compared to this earlier baseline and the simulated baseline result presented in plot, we found some

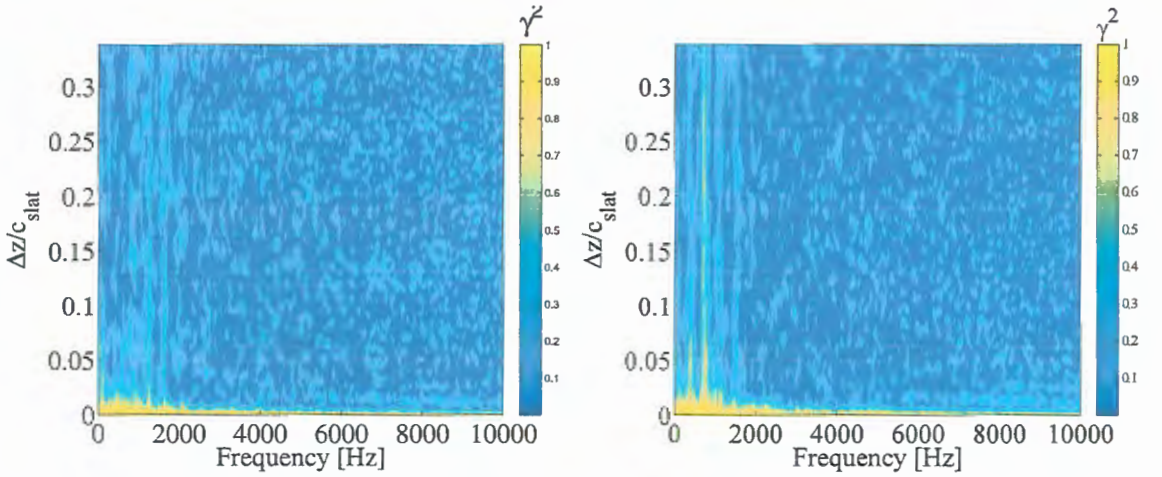

(a) Baseline (b) Seal 0.41 h3w3

Figure 17: Coherence level ($\gamma^2(\Delta z, f)$) over spanwise direction for baseline and sealed configuration 0.41 h3w3.

slightly higher peaks for sealed configuration. Despite of that, the maximum normalized coherence length presented the maximum level around 0.33 for seal 0.41 h3w3 which it is still considered a low coherence length related to slat chord. This result indicates that span length was enough to capture the tri-dimensional effects of simulations.

$$\gamma^2(f) = e^{-(\frac{\Delta z}{L_c(f)})^2}, \tag{4.2}$$

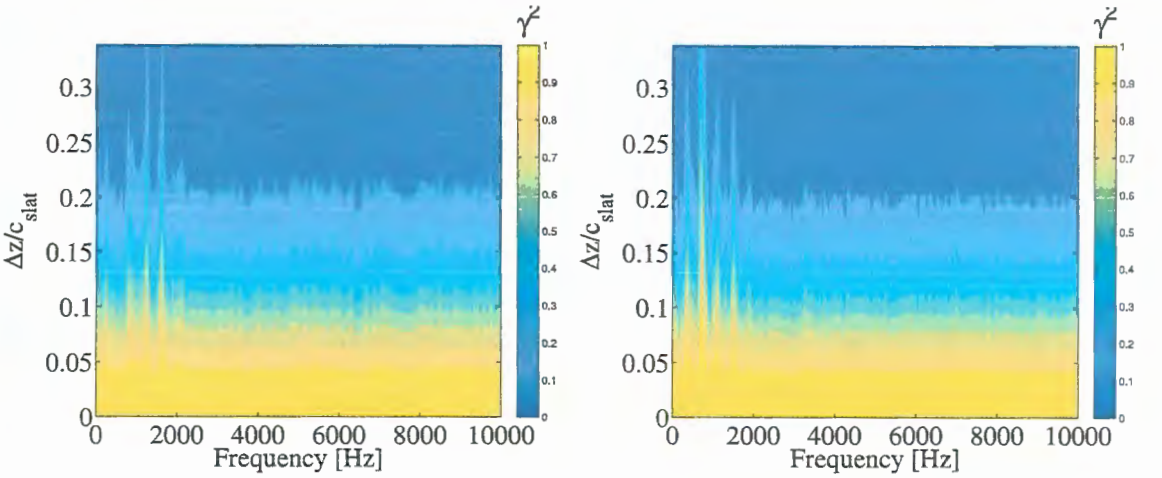

(a) Baseline (b) Seal 0.41 h3w3

Figure 18: Gaussian fit of coherence level ($\gamma^2(\Delta z, f)$) over spanwise direction for baseline and sealed configuration 0.41 h3w3.

A larger spanwise domain was also simulated and showed no significant changes. This result added to the coherence analysis presented above shows that the simulation

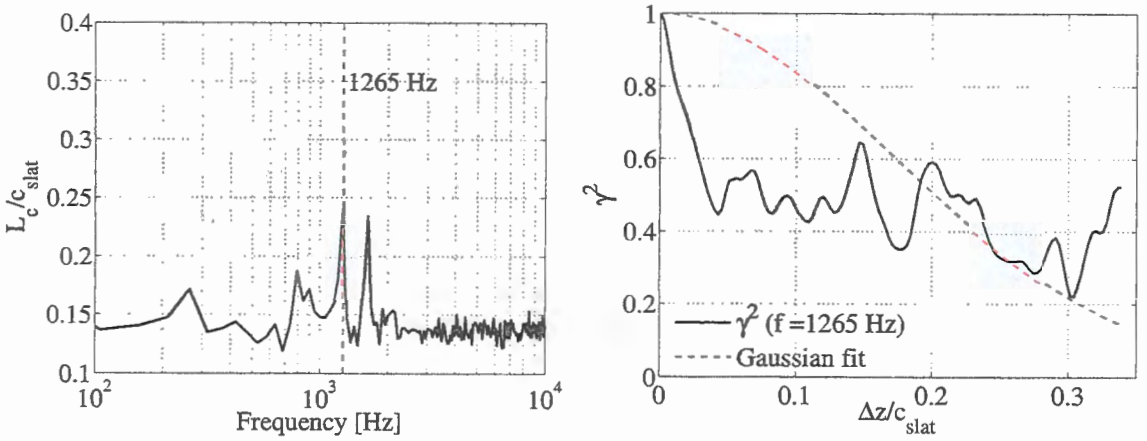

(a) Coherence length. (b) Coherence and Gaussian fit.

Figure 19: Coherence length and Gaussian fit curve of the most intense peak of baseline case.

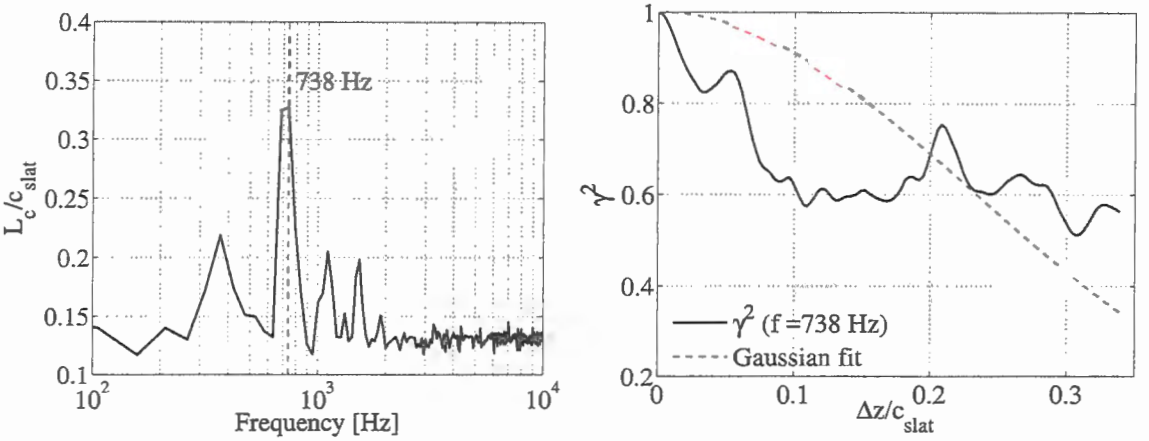

(a) Coherence length. (b) Coherence and Gaussian fit.

Figure 20: Coherence length and Gaussian fit curve of the most intense peak of sealed configuration 0.41 h3w3.

domain length in spanwise direction was enough to capture the tridimensional effects for this configuration that includes the seal.

Simulations were performed in a cluster with Xeon X5570 (quad-core, 2.93 GHz) processors. For the baseline configuration, approximately 16000 *CPU hours* were necessary to simulate 0.22 s of physical time, of which the initial 0.05 s were discarded. Such time periods were based on earlier studies (SIMÕES; SOUZA; MEDEIROS, 2011; SOUZA; RODRIGUEZ; MEDEIROS, 2013). For the seal configuration, the initial transient was longer, i.e., approximately 0.1 s, and the total simulation time corresponded to 0.25 s of physical time. The temporal evolution of the lift coefficient and its standard deviation (σ) are shown in Fig. 21, where the horizontal line indicates the mean of the statistically

converged results. The level of statistical convergence is similar to that of the previous baseline studies (SIMõES; SOUZA; MEDEIROS, 2011; SOUZA; RODRIGUEZ; MEDEIROS, 2013).

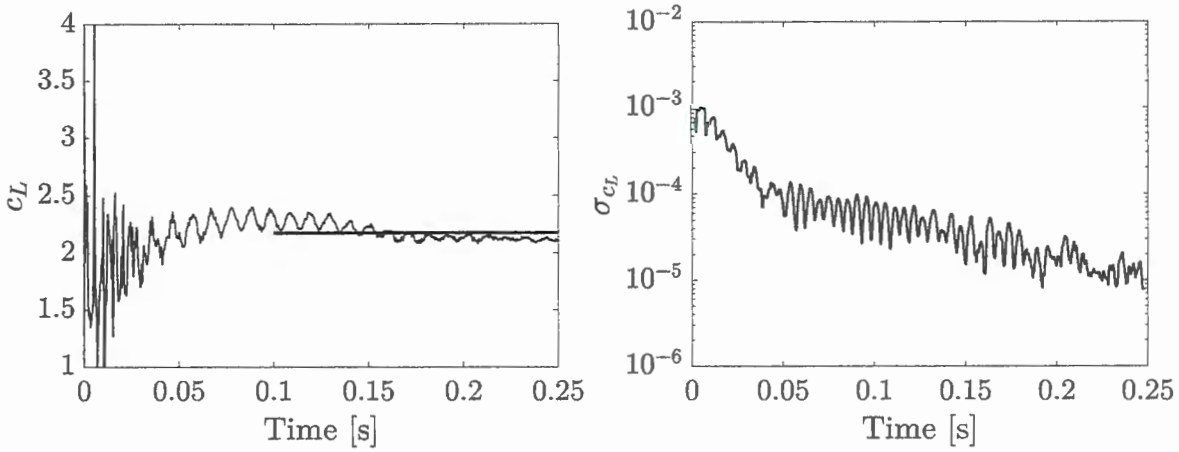

Figure 21: Time evolution of lift coefficient and its standard deviation (σ) for sealed case 0.41 h3w3.

The results of this section showed that simulation was converged in time, mesh and span. The intensity of the broadband peaks in far-field noise spectra, however, did not achieve the levels observed in experiments for seal 0.41. This indicates that the sealed configuration is more complex than baseline in which tonal peaks agreed well with experiments. Then, to investigate the reasons for this code inability, the sealed configuration was studied varying its position, height and airfoil angle of attack in order to understand the effects of this bulb seal on the slat cove flow dynamics.

5 NUMERICAL RESULTS

5.1 Cases Description

The numerical analysis considered angles of attack, seal positions and heights as presented bellow:

- Baseline:
  - AoA 3°;
  - AoA 7°;
- Seal 0.23:
  - AoA 3°, $h = 3\ mm$ and $w = 3\ mm$;
- Seal 0.41:
  - AoA 3°, $h = 1\ mm$ and $w = 3\ mm$;
  - AoA 3°, $h = 3\ mm$ and $w = 3\ mm$;
  - AoA 5°, $h = 3\ mm$ and $w = 3\ mm$;
  - AoA 7°, $h = 3\ mm$ and $w = 3\ mm$;
  - AoA 9°, $h = 3\ mm$ and $w = 3\ mm$;
- Seal 0.60:
  - AoA 3°, $h = 3\ mm$ and $w = 3\ mm$;

The chosen seal positions represent the most relevant noise regimes observed in the experiments (AMARAL, 2015). Positions 0.23 and 0.41 were within the quietest and noisiest regimes, respectively. Position 0.60 exhibited a different pattern in the low-frequency narrowband peak component, for which the second peak shows the highest noise levels, in contrast to the other seal positions, at which the first narrowband peak shows the highest noise levels. The seal geometry was squared sectioned with 3 mm edges, except for the position 0.41, for which a seal of 1 mm height was also studied. Configurations baseline and seal 0.41 were also simulated for different angles of attack.

For nomenclature, the cases will be refered as done before for seal 0.41, i.e., "*seal <position> h<height>w<width>*", where the position is the distance of the seal from slat

trailing edge normalized by slat chord and the values of height and width presented in mm unit. The angle of attack will be omitted in this nomenclature.

For far-field noise the Ffowcs Williams-Hawkings analogy was applied considering only the surfaces in the half center span of the slat and main element leading edge for integration. Time series were divided in blocks with 50% of overlap and a Hanning filter was applied before power spectrum calculation. The frequency resolution was around 50 Hz for each block and the Power Spectral Density (PSD) was the average of the blocks. The initial transient was discarded for all simulations and the useful time was around 0.15 s.

The mean flow analysis considered streamlines and 3D Turbulent Kinect Energy ($\frac{1}{2}(\overline{u'^2} + \overline{v'^2} + \overline{w'^2})$) are also presented to show the dynamics of structures inside the slat cove. For this analysis, the average of all realizations were taken in the central plane normal to spanwise direction.

The streamwise fluctuation velocity in near-field is also displayed in analysis at points $P1$, $P2$, $P3$ and $P5$ which represent, respectively, the 20%, 45%, 60% and 81% of mixing layer considering the case baseline at 4° of earlier study on baseline (SOUZA, 2012). These points were considered for this analysis because the variation of arfoil angle of attack for 3° does not change the mixing layer considerably, then their positions were considered to avoid a previous simulation for the exact mixing layer determination. For high angles, however, this was not a good approximation since the results here presented considered angles until 9° degrees and at this angle the recirculation region shrinks considerably and the probes were located outside the mixing layer. However the results are still presented for visualization.

5.2 Seal position effect

Figure 22 presents a comparison of simulation cases varying the seal position on slat cove. Experimental data presented by Amaral (2015). The results show that c_P over airfoil is not affected by seal presence for main element and flap but only for the slat cove region in region between the seal and trailing edge. This mean that only structures in nearfield region of the slat are affected by this excrescence but total airfoil lift are not affected significantly. The numerical results also presents boundary layer separation on flap surface that not occurs in experiments. This may be related to the fully turbulent boundary layer assumption made by code.

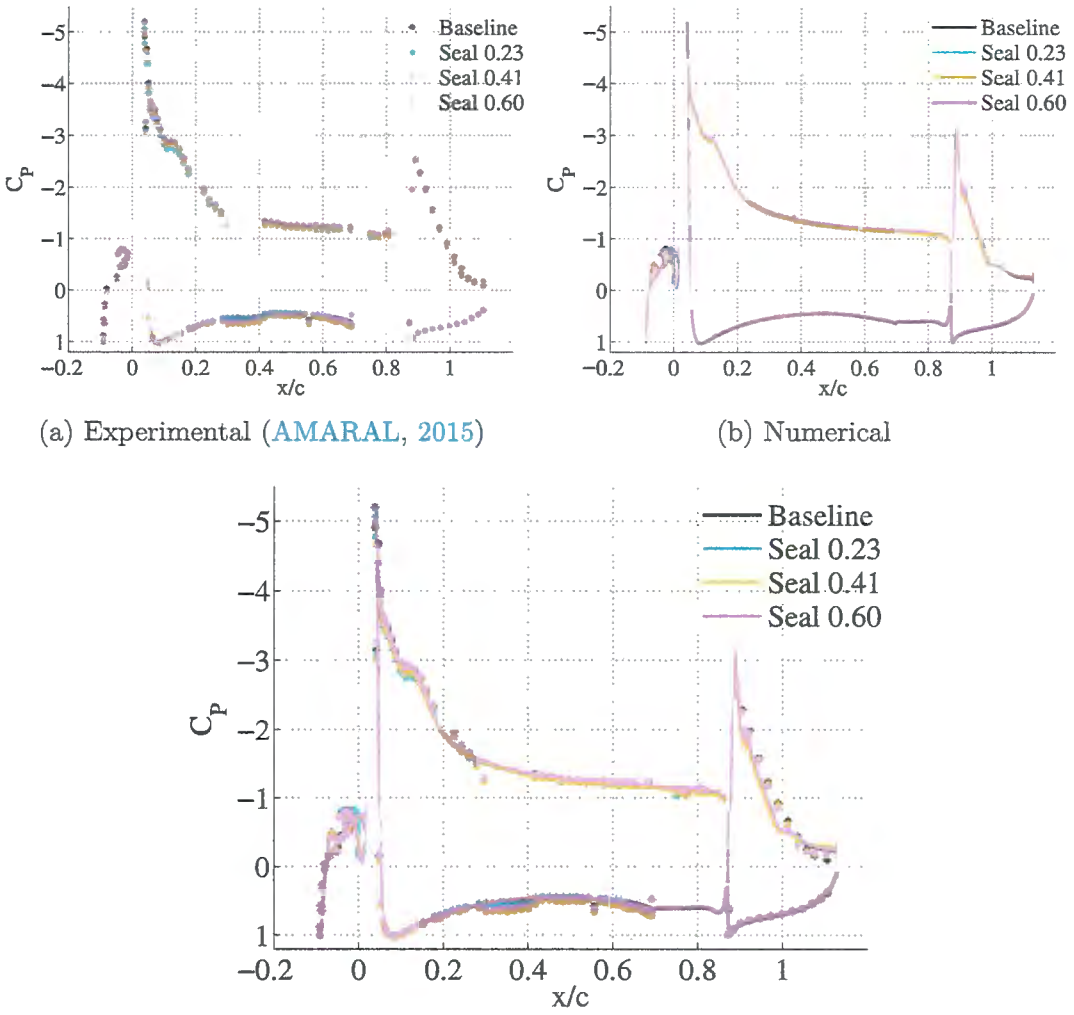

(a) Experimental (AMARAL, 2015)

(b) Numerical

(c) Comparison

Figure 22: Experimental and Numerical c_P for baseline and sealed cases. AoA 3° and seal h3w3.

Farfield noise spectra are presented in Fig. 23 and 24 showing the comparison between numerical and experimental data (AMARAL, 2015). Numerical results shows a

good comparison with experiments for baseline and 0.23 cases but for sealed geometries 0.41 and 0.60, the intensity of the tonal peaks were not well reproduced. However, peaks frequencies of this cases agreed reasonably well with experiments including the frequency shift in case 0.41. Configuration 0.60 also presents a curious effect, the second peak is the most intense in experiments. Simulations could not reproduce this effect clearly but indicates the same intensity level of the first peak differently than other cases.

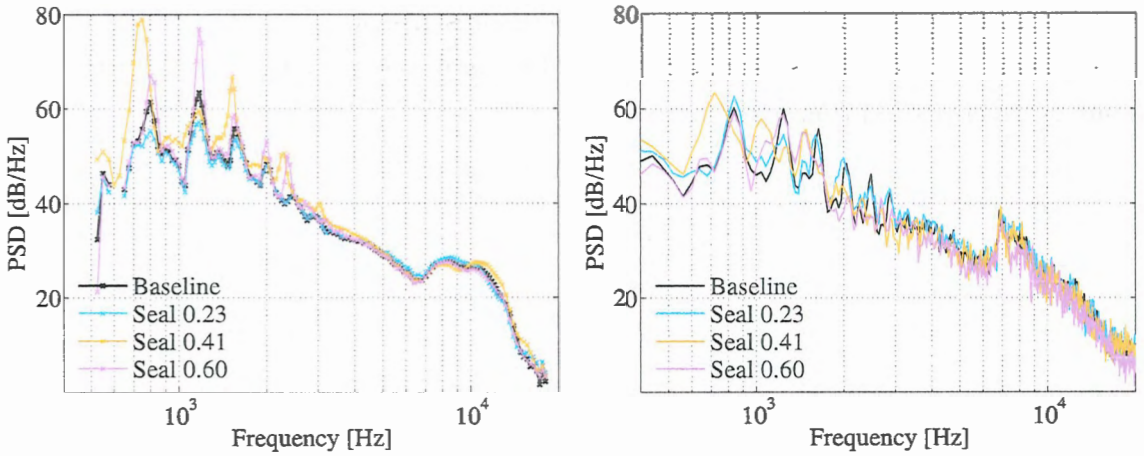

(a) Experimental. (b) Numerical

Figure 23: Experimental (AMARAL, 2015) and Numerical far-field noise spectra presented for baseline and sealed geometries varyng its position inside cove. $AoA = 3°$, seal h3w3

The meanflow field are present in Fig. 25 to understand the differences observed in farfield noise spectra. The streamlines and resolved 3D TKE shows that is possible to identify two categories of cove flow dynamics: first with only one recirculation and the second with additional counter-rotating recirculation. Baseline and seal at position 0.23 are in the first category and cases with seal at 0.41 and 0.60 in the second one. According to noise spectra, the first category represent the quieter and second, the noisier cases considering the tonal peaks levels. It is also noted that the seal presence cleans the region near to cusp from turbulence generated in reattachment point. This behaviour is even noticed in the case 0.23 compared to baseline one but did not influenced in the propagated noise as seen earlier in noise spectra. For cases 0.41 and 0.60, the second bubble increased the turbulence level at earlier stages of reattachment point across shear layer. The effect of seal working as a barrier from turbulence across cove wall are also noted but in this category of cases, the turbulence travels through the mixing layer between two recirculations from seal to slat cusp.

The fluctuation of the streamwise velocity are presented in Figures 39 and 27, comparing the results for each position and other presenting the evolution in mixing layer of the fluctuation for each case. Results shows a clear difference of the two categories of cases observed in mean flow contour plots.

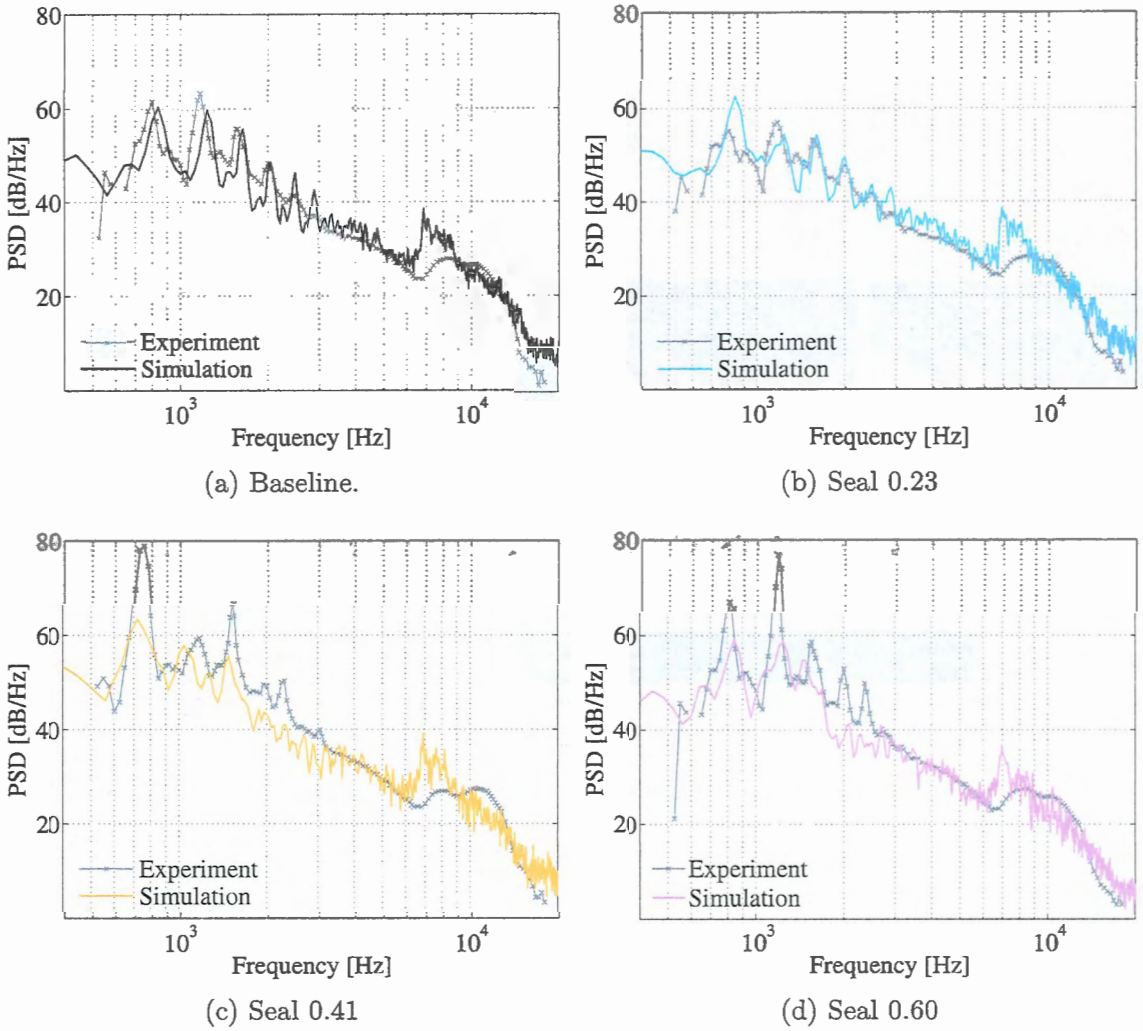

(a) Baseline.

(b) Seal 0.23

(c) Seal 0.41

(d) Seal 0.60

Figure 24: Comparison of Experimental (AMARAL, 2015) and Numerical far-field noise spectra for baseline and sealed geometries varyng its position inside cove for each configuration. $AoA = 3°$, seal h3w3

Configurations with only one bubble shows a development of the fluctuations from high frequency band to low frequency band with intensification of peaks. The other category with two bubbles, presents a higher fluctuation and peaks since earlier stages of mixing layer. The turbulence cleaning effect of seal is observed for case 0.23 compared to baseline. At earlier stages (P1) of mixing layer, the intensity of peaks seems higher for sealed configuration but they achieve the same levels of baseline ones but broadband component is lower, indicating less turbulence at this region. Some curious behaviour is observed between the 0.41 and 0.60 configurations that are similar at initial stages of mixing layer but for latter steges, 0.60 is much closer to that presented by the baseline and 0.23. Thus, the 0.60 case is peculiar in that it presents an aspect of both the baseline and seal 0.41.

For most intense peaks in far-field noise spectra, POD analysis was applied using

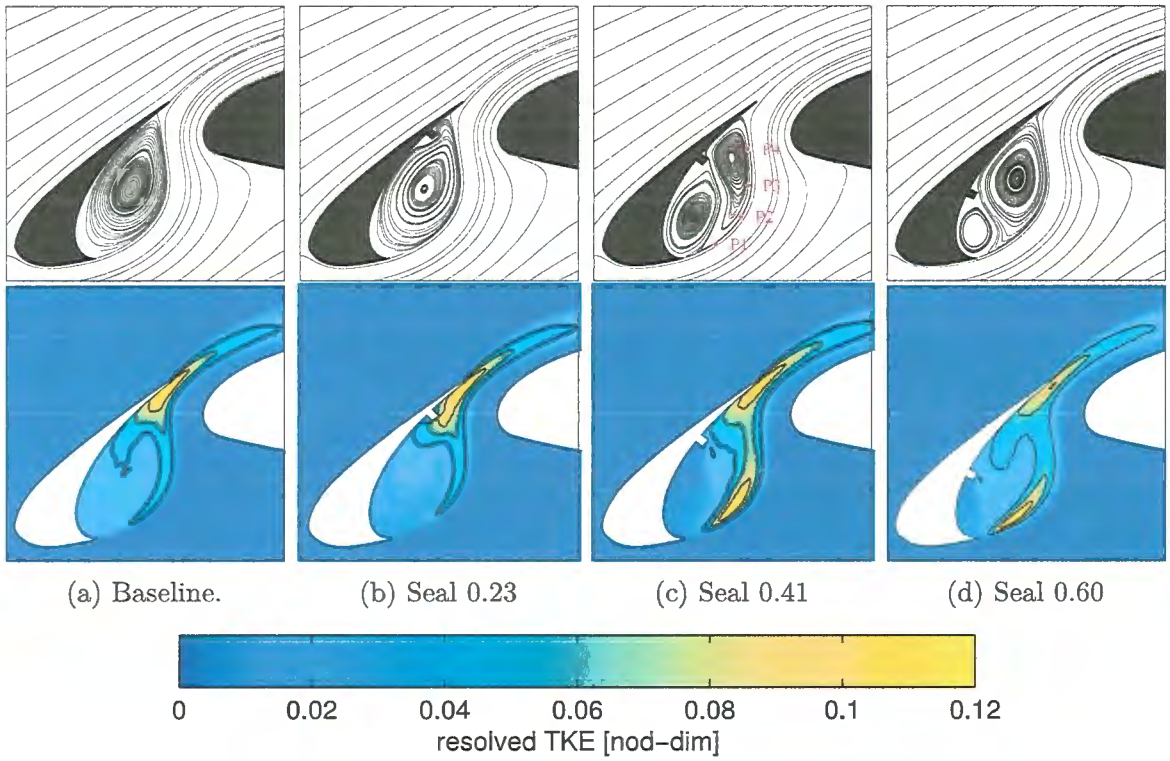

Figure 25: Streamlines and resolved TKE for clean and seal cases. $AoA = 3°$, seal h3w3.

the far-field pressure inner product (P_{Pff}). Figure 28 shows the first and second peaks of cases baseline and sealed one varying its position. The frequencies for POD calculation is presented in red and blue dotted curves for seal 0.41 and other cases. The eigenvalues normalized by the sum of all eigenvalues are presented in Fig. 29 showing the relevance of the first POD mode. Figures 30 and 31 shows the real part of POD mode for this first two peaks.

Baseline displays the most intense structures in the mixing layer near the region of the reattachment point. This corroborates the results obtained in previous works (SOUZA et al., 2015). The seal inclusion changes this trend but in a particular way for each case. For seal 0.23, the results closely approximate the baseline, as expected by earlier observation of mean flow and near-field fluctuation spectra. For seal 0.41, POD shows structures much more coherent and present in almost the fully extention of the mixing layer compared to the baseline. Seal 0.60 case represents a combination of the baseline and seal 0.41, presenting structures less intense for the first peak as the baseline but intensifying the second peak as seal 0.41. This characteristic was also evidenced in the study of velocity fluctuations in the near field.

Results from Souza (2016) shows a feedback mechanism on slat cove similar to that observed for (MANOHA et al., 2012) which was a Rossiter mechanism adapted to slat. This results show that Rossiter mode could be determined by the simple counting of

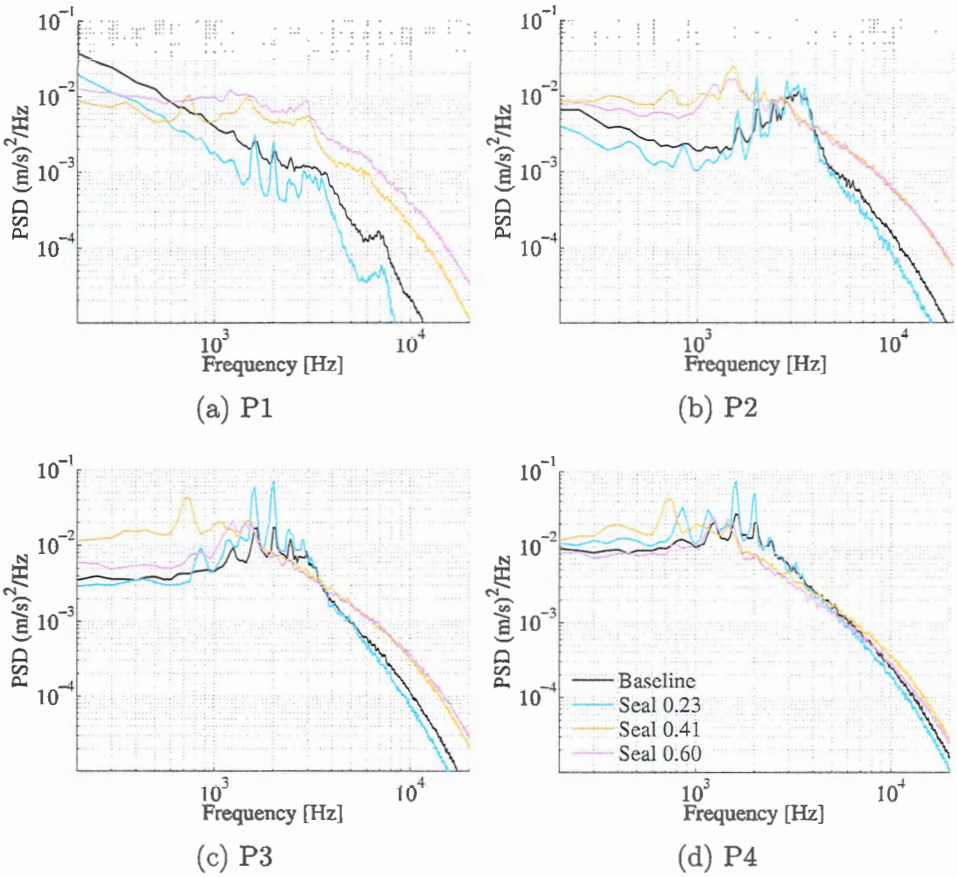

Figure 26: Streamwise fluctuation velocity along mixing layer for each case (see Fig 25 for points reference). $AoA = 3°$, seal h3w3.

structures cycles on the mixing layer. Then, we can identify that the first two most intense peaks presented for baseline and sealed cases are the second and third Rossiter modes, respectivelly.

Linear Stability Theory was applied to investigate the behaviour of the most unstable modes of the mixing layer from the cusp to the reattachment point. Figure 32 shows the velocity profile of the simulations (black curves) with their respective approximation using the hyperbolic tangent function (red). Vorticity thicknesses are also shown for certain mixing layer positions. The tanh approximation seems reasonable well.

The evolution of the vorticity thickness for the base cases and with seals is presented in Fig. 33. For baseline and seal 0.23, the fluctuations evolution are very similar which corroborates the results of the near-field in which the results indicated much similarity to the baseline. The cases 0.41 and 0.60, however, present a greater vorticity thickness than the case without seal and their evolutions differ from each other. The increased vorticity thickness means longer wavelengths and therefore, lower frequencies for more unstable modes. This could explain why the noise spectrum peaks in the 0.41 configuration shows lower frequencies peaks.

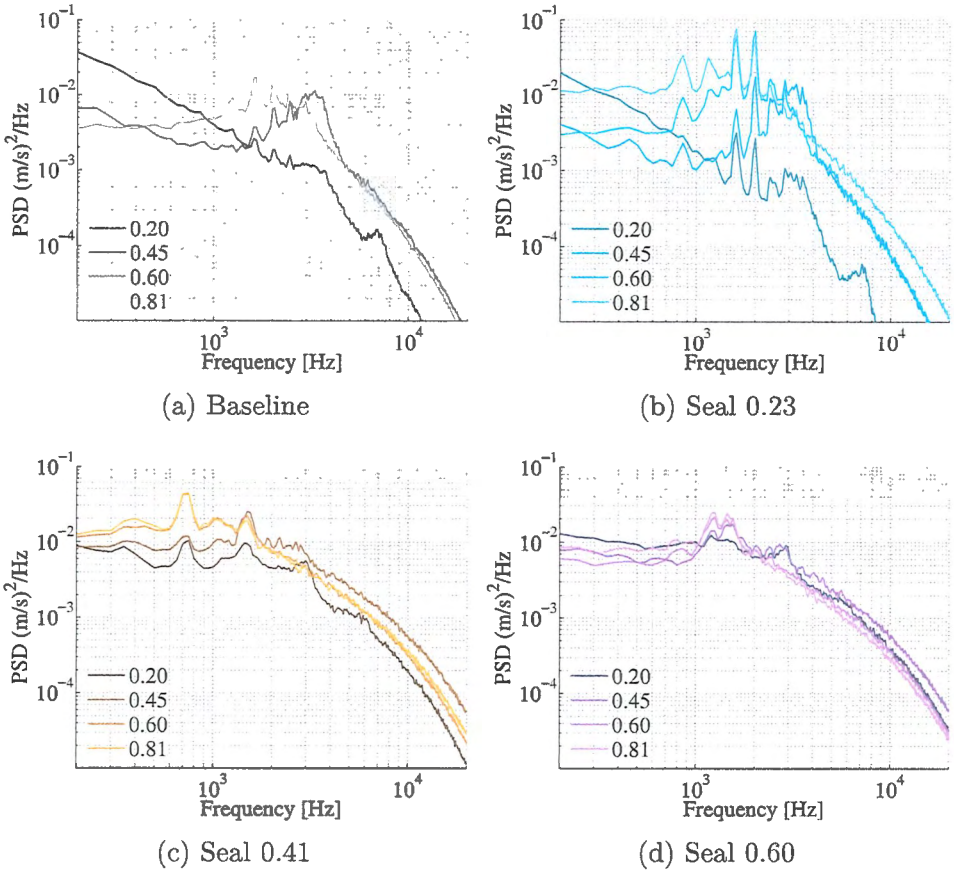

(a) Baseline (b) Seal 0.23

(c) Seal 0.41 (d) Seal 0.60

Figure 27: Streamwise fluctuation velocity along mixing layer comparing cases. $AoA = 3°$, seal h3w3.

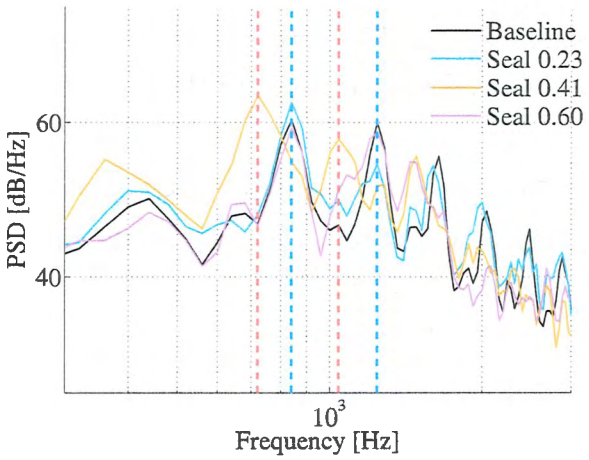

Figure 28: Far-field noise spectra showing the two most intense peaks of baseline and sealed configurations. Red lines correspond to frequencies $f = 720\ Hz$ and $f = 1040\ Hz$. Blue lines to frequencies $f = 840\ Hz$ and $f = 1240\ Hz$, respectivelly. $AoA = 3°$, seal h3w3.

For seal 0.60, however, the same conclusion does not apply. In fact, as discussed in the near-field analysis, the 0.60 case has similarities to both the 0.41 case (at the beginning

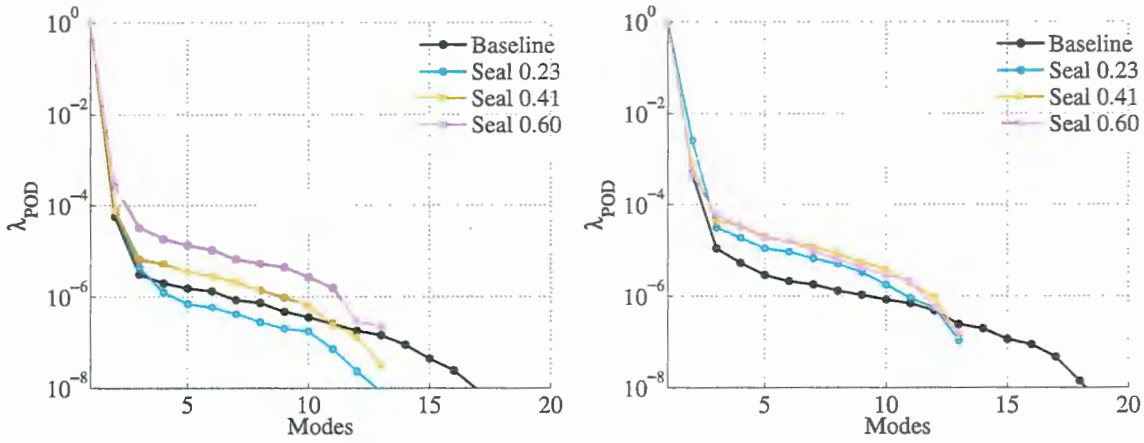

(a) First POD mode (b) Second POD mode

Figure 29: Normalized eigenvalues of POD using far-field pressure inner product (P_{Pff}) in the frequencies of two most intense peaks of baseline and sealed configurations varying its position (See Fig. 28). $AoA = 3°$, seal h3w3.

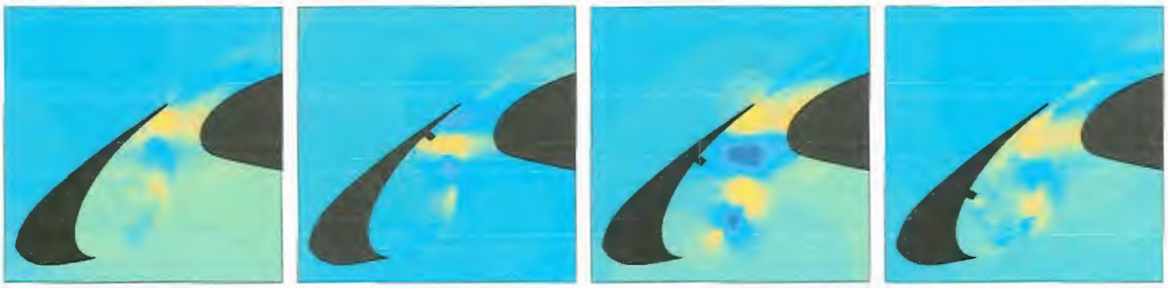

(a) Baseline (b) Seal 0.23 (c) Seal 0.41 (d) Seal 0.60

Figure 30: Real part of first POD mode of first peak in far-field noise spectra for baseline and sealed cases. Far-field pressure inner product (P_{Pff}). $AoA = 3°$, seal h3w3.

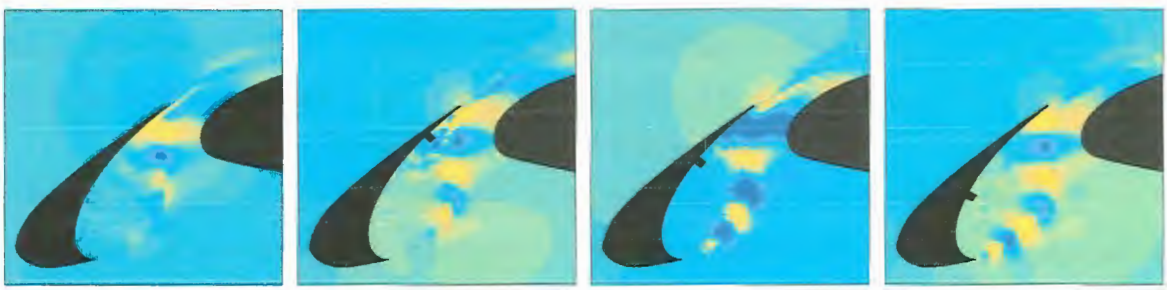

(a) Baseline (b) Seal 0.23 (c) Seal 0.41 (d) Seal 0.60

Figure 31: Real part of second POD mode of first peak in far-field noise spectra for baseline and sealed cases. Far-field pressure inner product (P_{Pff}). $AoA = 3°$, seal h3w3.

of the mixing layer) and the baseline or 0.23 (at final stages). In fact, the vorticity thickness indicates a plateau just before reattachment and then a similar thickness increase rate as that of the case with one single bubble. The decrease in the frequency of noise peaks in

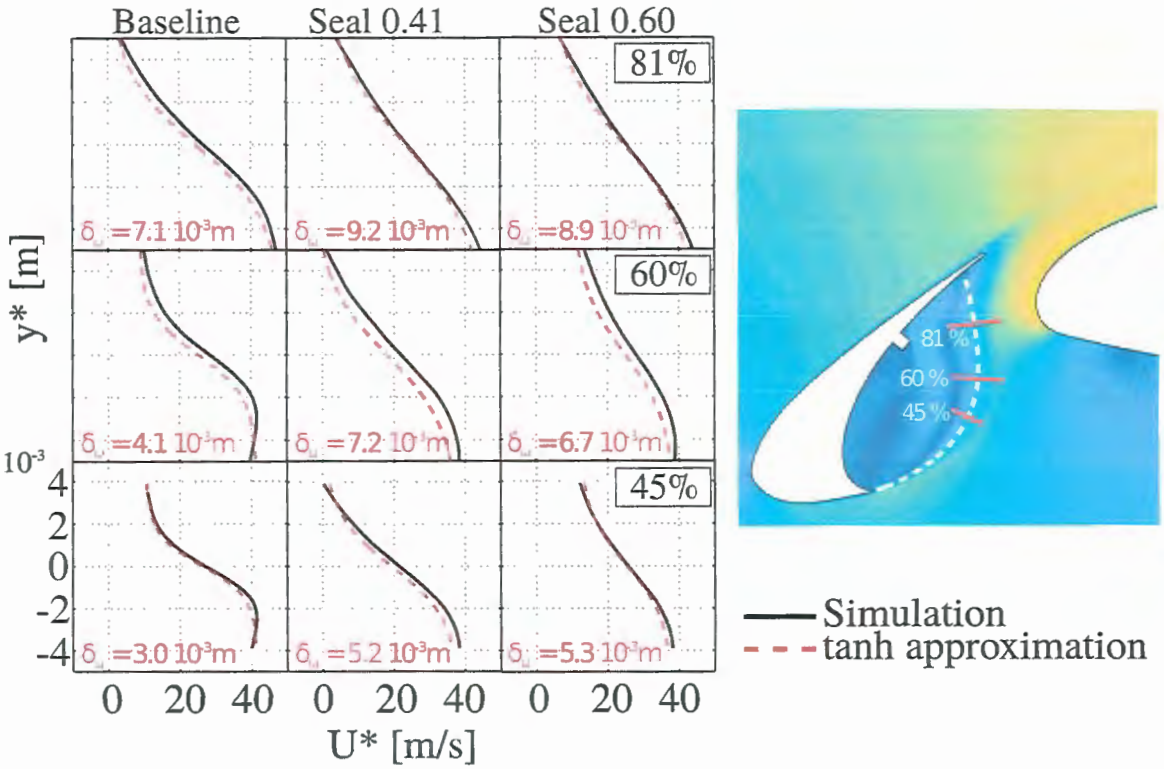

Figure 32: Comparison between the velocity profile and the tanh approximation perpendicular to the sections 45%, 60% and 81% (red lines) indicated in the mixing layer (dashed white curve).

the far-field, however, are not observed indicating a more complex phenomenon.

The most unstable frequencies of the mixing layer were calculated similar to that presented by Deck e Laraufie (2013) in the early stages of the mixing layer and presented good results. In this theory, a parallel flow hypothesis is used which makes it impossible to analyze regions of cases 0.41 and 0.60 in which the presence of the secondary bubble deforms the main recirculation and makes the flow non-parallel. Thus, only the continuous region of the graph 33 is used for analysis with the LST theory.

Figure 34 shows the velocity fluctuation spectrum in the streamwise direction at certain positions of the mixing layer and its respective most unstable frequency and theoretical amplitude. For the calculation of the theoretical amplitude, a flat signal was given as input as shown in the first graph of each case. Then, the evolution of the amplitude of the fluctuations can be given by Eq. 3.55, where L_0 is the first position considered for integration and L, the position at which the amplitude is being calculated.

The increasing of mixing layer thickness makes the most unstables frequencies shift from high to low frequency band. The mixing layer development makes the fluctuations amplitude, which depends on the integral of the amplification rates, goes from a hump in the high frequency to the low frequency. This is similar to that observed in near-field spectra

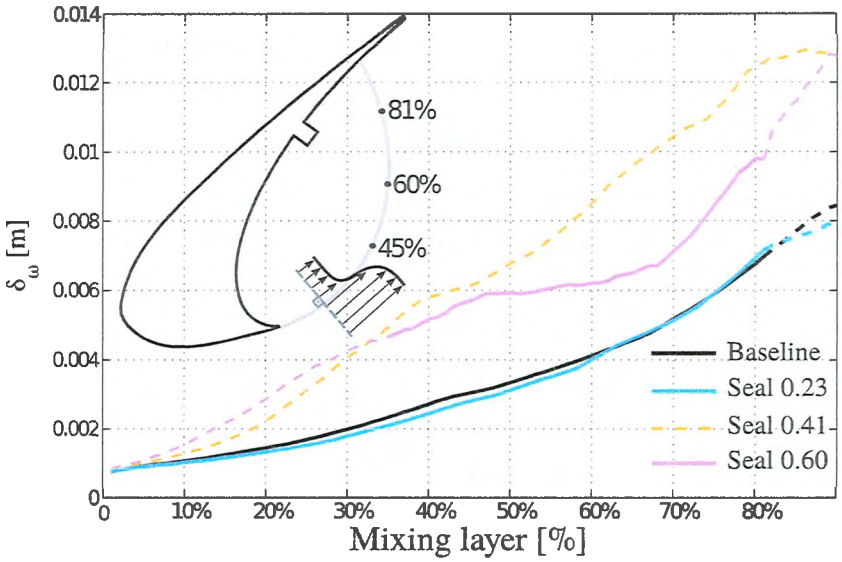

Figure 33: Evolution of the vorticity thickness considering speed profile as being a tanh function. Dashed lines indicate the region in which the study of the most unstable modes by the LST was not applied because they violate the hypothesis of parallel flow, allowing only the analysis of δ_ω.

for baseline and seal 0.23, which indicates that this pattern is related to a phenomenon of the evolution of the mixing layer itself.

The peaks that appear above these broadband fluctuations and which may be directly related to the noise peaks in the far-field, we can verify that they are within the amplified band and therefore also receive a contribution of this phenomenon but the intensity of the tonal is not explained by the LST or, at least, not directly. It is much more likely that the tonal peaks are related to the Rossiter modes that occur in the cove (KOLB et al., 2007b; MANOHA et al., 2012; SOUZA et al., 2015).

The 0.60 case presents a different behavior from the baseline and the LST analysis does not shows reasonable results. As the initial stages of the mixing layer present non-parallel flow due to the deformation of the bubble, the theory is only applied to advanced stages of the same. Even so, the behavior of the velocity fluctuations intensity practically does not change and are more similar with the final stages of the baseline. This indicates that the structures convected by the region between bubbles insert certain turbulence into the mixing layer in order to create a more intense mechanism than that observed for the baseline. This feature advances the behaviour of the mixing layer and the entire frequency band is amplified regardless of the most unstable frequency of the mixing layer.

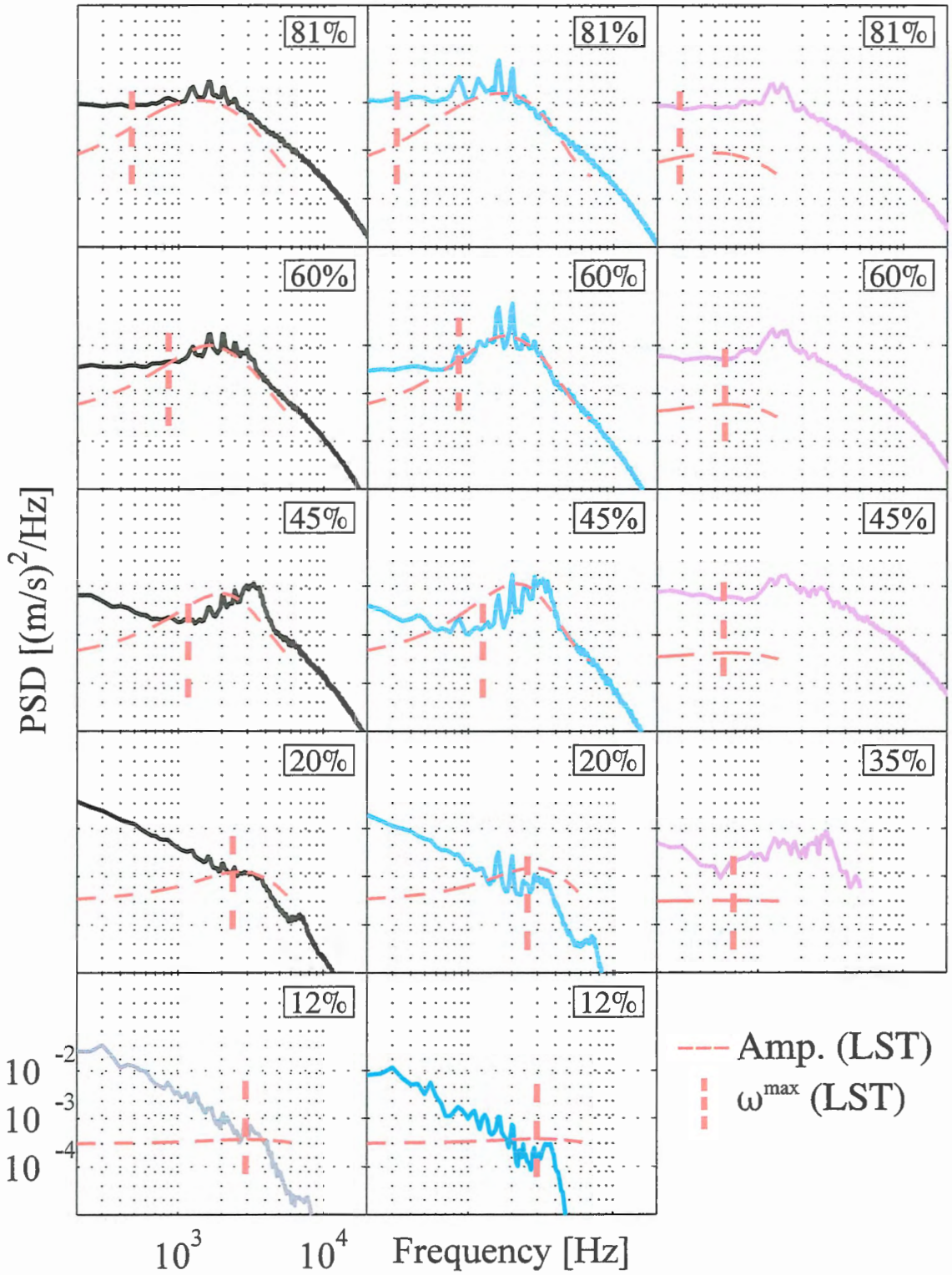

Figure 34: Streamwise velocity fluctuation along the mixing layer. Initial position for amplitude calculation was 12% (base and seal 0.23) and 35% (seal 0.60) to respect the parallel flow hypothesis.

5.3 Angle of attack effect

This section presents the analysis of the seal effect varying the angle of attack which were 3°, 5°, 7° and 9°. The seal dimension and position inside cove wall were constant, i.e., seal h3w3 at position $d = 0.41$.

Following the earlier section, simulation results are compared to experimental work of Amaral (2015). Pressure coefficients distribution over airfoil are presented in Fig. 35. Simulations c_P agreed reasonably well with experiments for cases presented but the intensity of suction peak is subestimated in simulations. The numerical results also presents boundary layer separation on flap surface that not occurs for experimental data, except for angle of attack 9°. This fact may be related to the fully turbulent boundary layer assumption made by code as cited in earlier section.

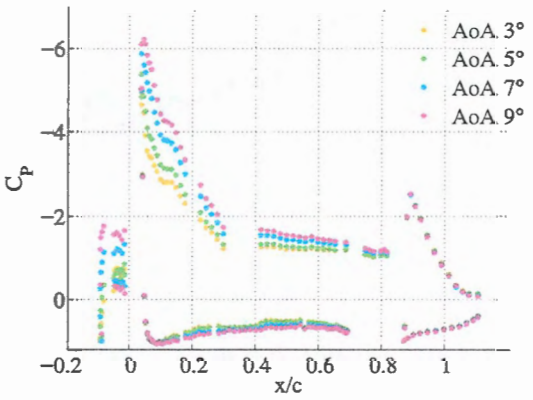

(a) Experimental (AMARAL, 2015)

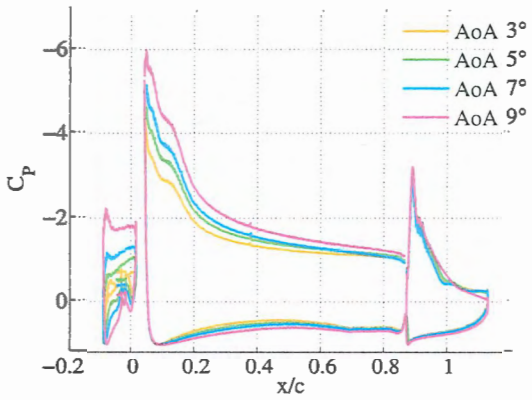

(b) Numerical

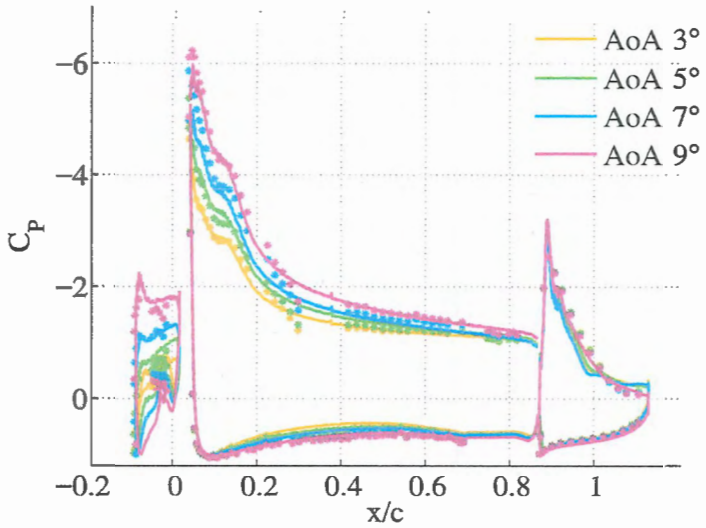

(c) Comparison

Figure 35: Experimental and Numerical c_P for baseline and sealed cases varyng airfoil angle of attack. Seal 0.41 h3w3.

Far-field noise spectra is presented in Fig. 37 and 37 both experimentally and numerically for comparison. As observed in seal position section, we observe proeminents peaks in broad-band frequency that simulations did not reproduce. However, as the angle of attack increases the intensity of these peaks reduces for simulation as observed in experimental data provided by Amaral (2015) and also in earlier studies (KOLB et al., 2007a; IMAMURA et al., 2009; PAGANI JR; SOUZA; MEDEIROS, 2016). Some curious result that is highlighted by the less intense peaks in simulations is the presence of lower peaks in the neighbour region of the most intense peaks. In experiments these "sub-peaks" do not appears clearly for the noisiest configurations but they are observed in cases of higher angles of attack such as 9°.

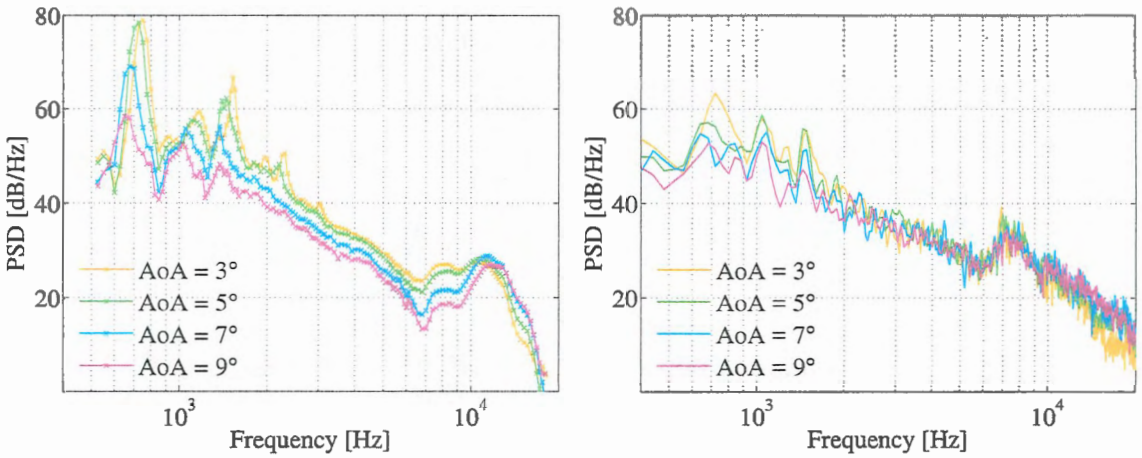

(a) Experimental (AMARAL, 2015). (b) Numerical

Figure 36: Experimental and Numerical far-field noise spectra presented for baseline and sealed geometries varyng airfoil angle of attack. Seal 0.41 h3w3.

The mean flow were also studied for these cases. The streamlines and resolve TKE are presented in Fig. 38 showing the same effect observed in earlier section for seal h3w3. The additional counter-rotating bubble is present in all angles of attack except for case at 9°. The angle increasing also reduces the intensity of TKE in mixing layer and for angle where the secondary bubble are not present, this region in mixing layer of higher TKE level is not present as expected. Then, configuration 9° presents results very similar to that observed for one-bubble cases presented in earlier section.

The near-field streamwise velocity is also presented in Fig. 39 and 40. But, since the data collected signals at same positions related to slat than that for earlier section, the variation of angle of attack shrinked the recirculation region and thus, the points $P(1, 2, \ldots, 4)$ are not exactly on the mixing layer for higher angles. We consider, however, that the points are closer enough to analysis of the behaviour and develpment of this evolution once, the fluctuations of the mixing layer itself affects its neighbour region. But the intensity of the fluctuations can not be compared directly. Then, the development

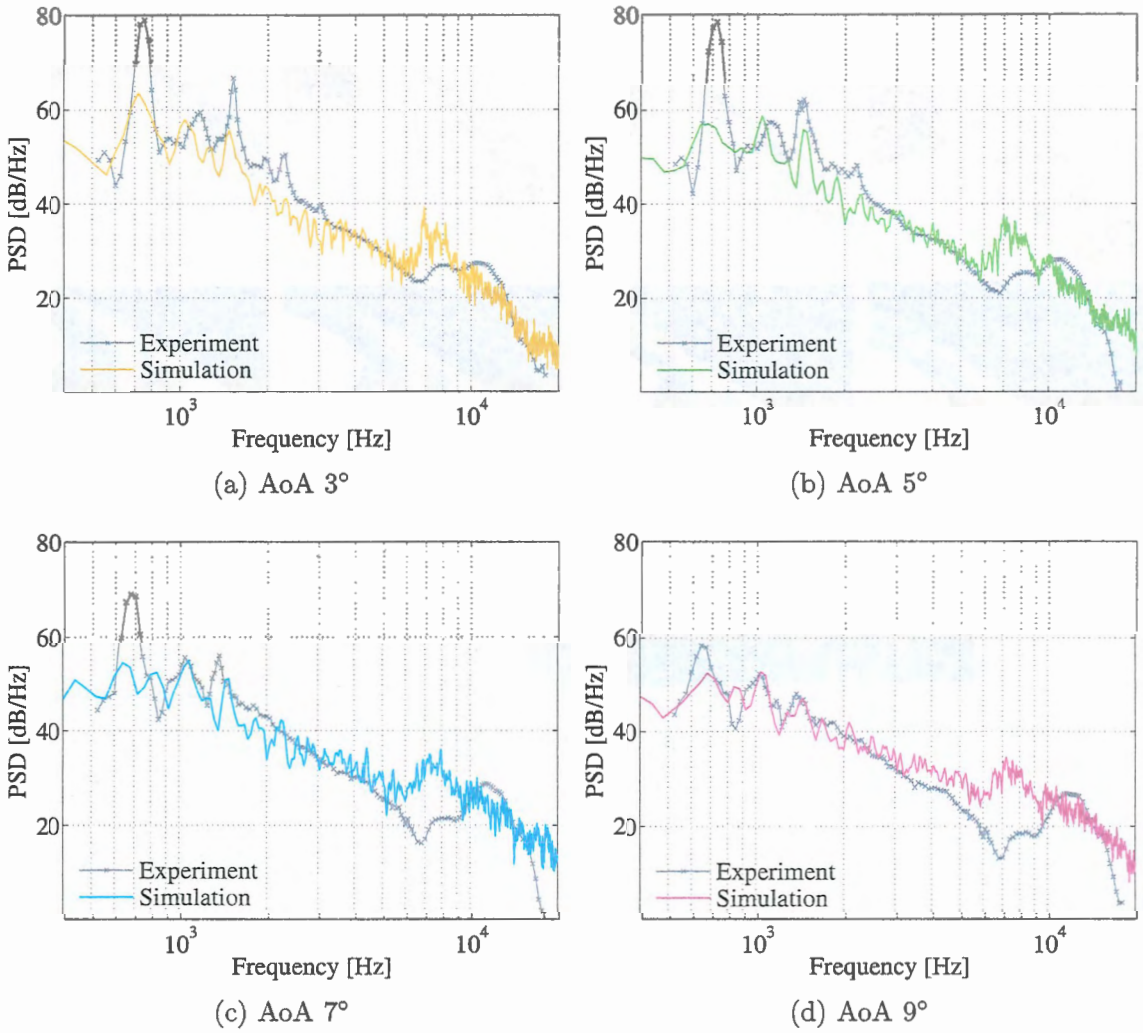

(a) AoA 3° (b) AoA 5°

(c) AoA 7° (d) AoA 9°

Figure 37: Comparison of Experimental (AMARAL, 2015) and Numerical far-field noise spectra for baseline and sealed geometries varyng airfoil angle of attack. Seal 0.41 h3w3.

of streamwise velocity on the mixing layer shows that the peaks are present basically at same frequencies but, as the angle of attack increases, the peak which frequency is around $f = 720\ Hz$ is less intense and the one around $f = 1240\ Hz$ is still more intense for angle 5°. For higher angles, the peak with frequency $f = 1040\ Hz$ presents a higher intensity comparable to that at $f = 1240\ Hz$ or even higher at 9°. This behaviour seems to be related to the sub-peaks observed in far-field noise spectra and some explanation could be given by interaction of some subharmonic phenomena.

The POD studies proceeds in same way as the seal position analysis. First the peaks of noise spectra are identified in Fig 41 for all angles simulated. Since the first more intense peak has the tendency to shift to lower frequencies as angle increases, the POD calculation considered a mean frequency ($f = 680\ Hz$) for angles 5°, 7° and 9°. For 3°, the first peak was considered at same frequency of earlier section, i.e., $f = 720\ Hz$. The second more intense tonal noise was considered the same for all angles, $f = 1040\ Hz$.

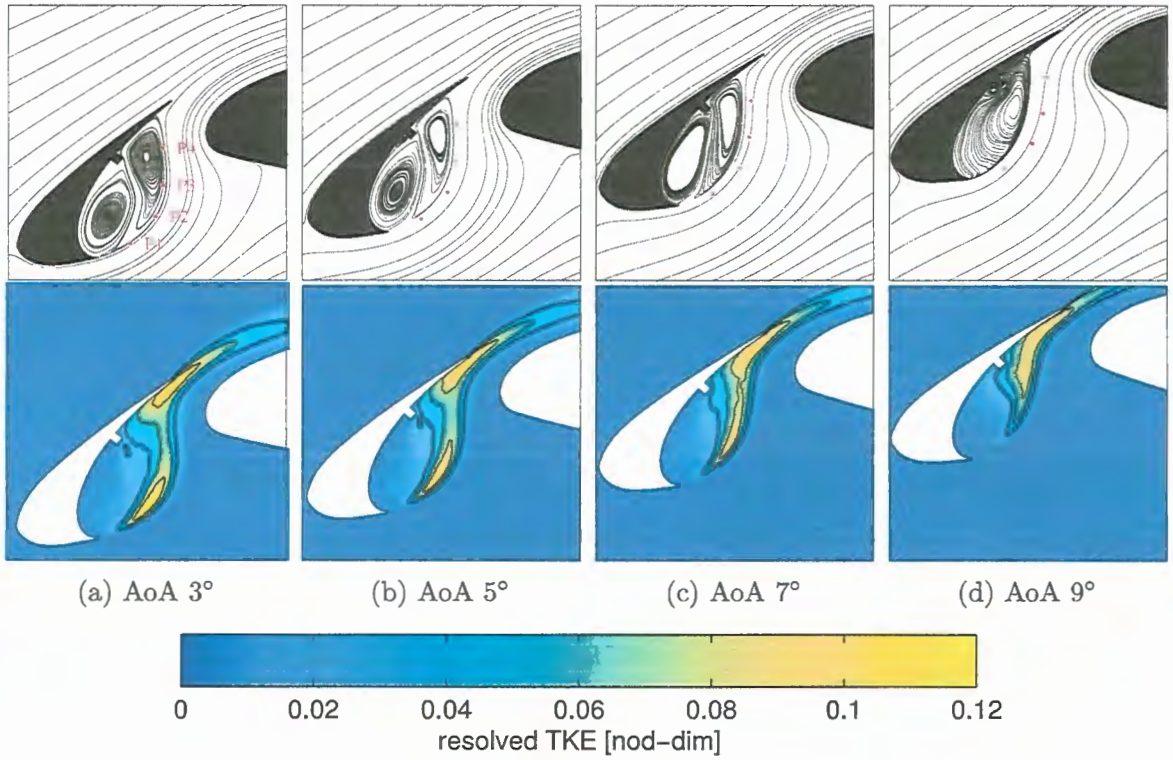

Figure 38: Streamlines and resolved TKE for clean and seal cases varyng airfoil angle of attack. Seal 0.41 h3w3

The normalized eigenvalues are presented in Fig. 42 showing that most representative mode is the first one. The results of POD are displayed in Fig. 43 and 44 showing a similar behaviour to all angles of attack. The large scales strutures become more intense closer the reattachment point for the first peak. For the second peak the structures are less defined. For higher angles such as 7° and 9° is also observed that structures are composed of two centers and this may be related to the mixing layer velocity gradient that changes the velocity of convection of the structures.

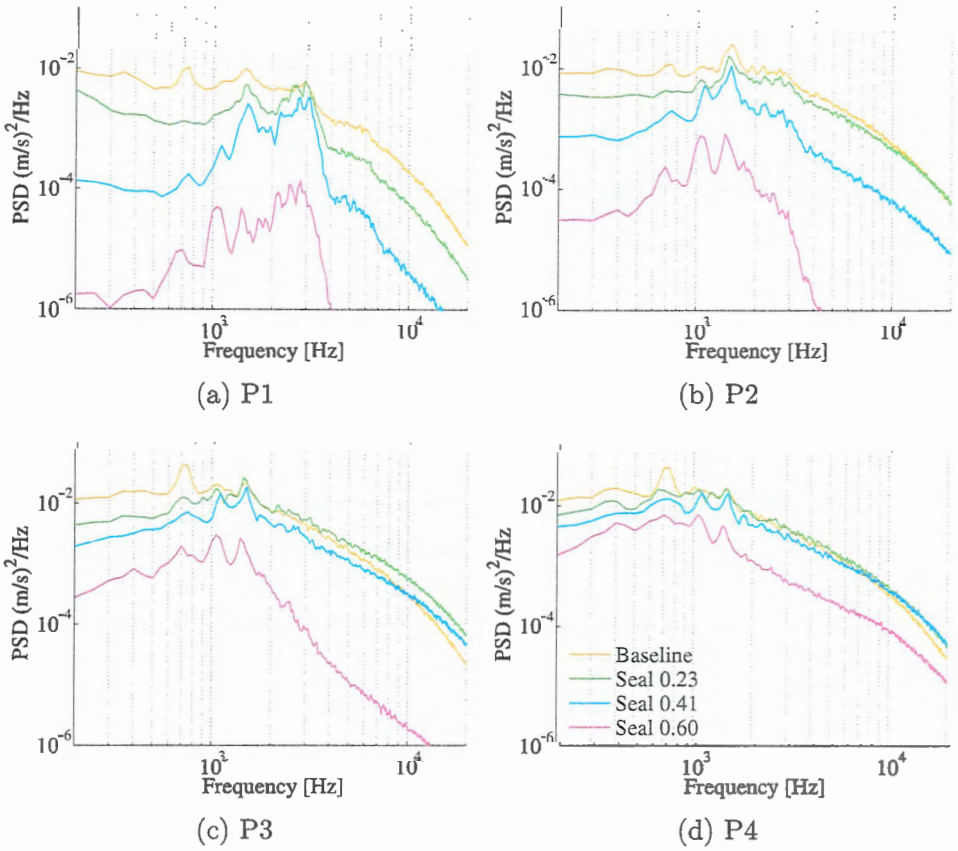

(a) P1 (b) P2

(c) P3 (d) P4

Figure 39: Streamwise fluctuation velocity along mixing layer at positions Pi (See Fig. 38 for points reference). $AoA = 3°$, seal h3w3.

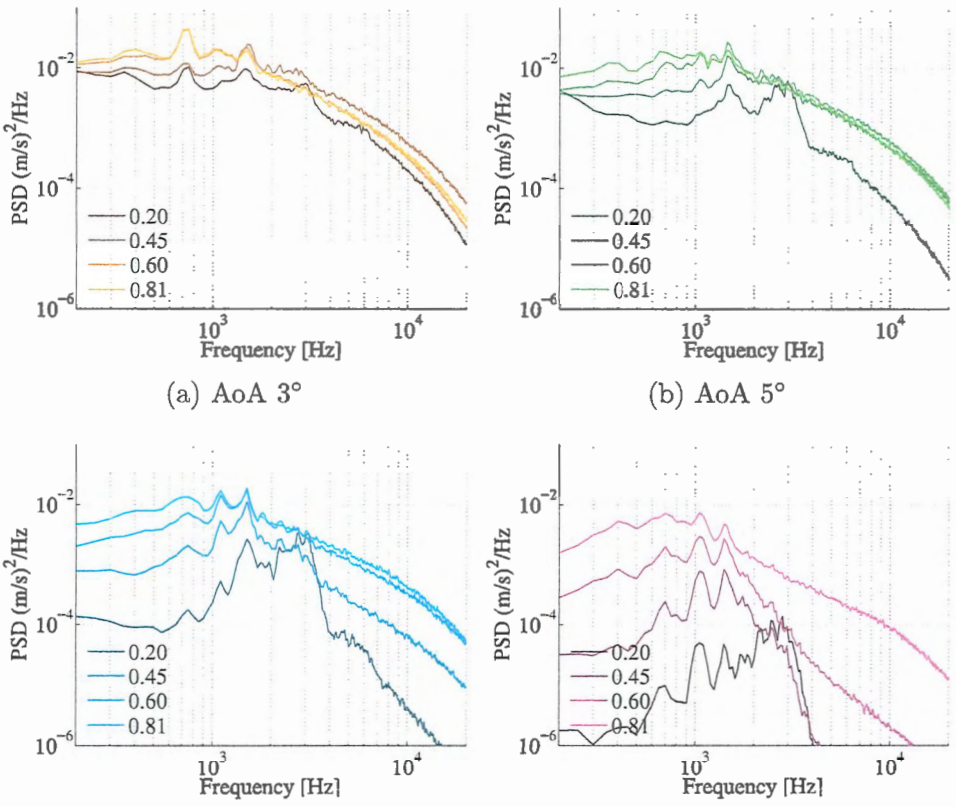

(a) AoA 3° (b) AoA 5°

(c) AoA 7° (d) AoA 9°

Figure 40: Streamwise fluctuation velocity along mixing layer varying angle of attack of the airfoil. Seal 0.41 h3w3.

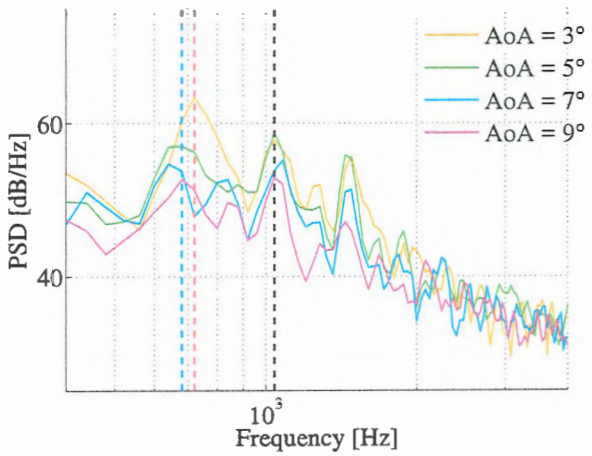

Figure 41: Far-field noise spectra showing the two most intense peaks of baseline and sealed configurations. Red line correspond to frequency $f = 720\ Hz$, blue, $f = 680\ Hz$ and black to frequency $f = 1040\ Hz$. Seal 0.41 h3w3.

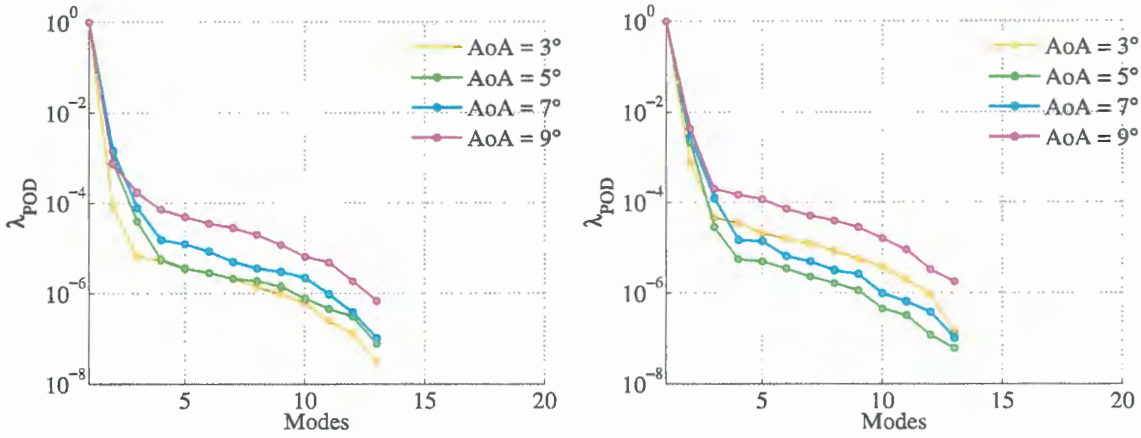

(a) First POD mode (b) Second POD mode

Figure 42: Normalized eigenvalues of POD using far-field pressure inner product (P_{Pff}) in the frequencies of two most intense peaks of sealed configurations varying angle of attack (See Fig. 41). seal 0.41 h3w3.

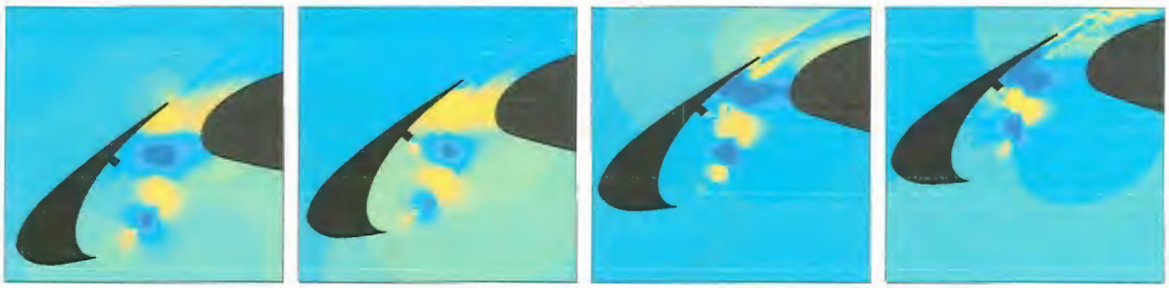

(a) AoA 3° (b) AoA 5° (c) AoA 7° (d) AoA 9°

Figure 43: Real part of first POD mode of first peak in far-field noise spectra sealed cases varying angle of attack. Far-field pressure inner product (P_{Pff}). Seal 0.41 h3w3.

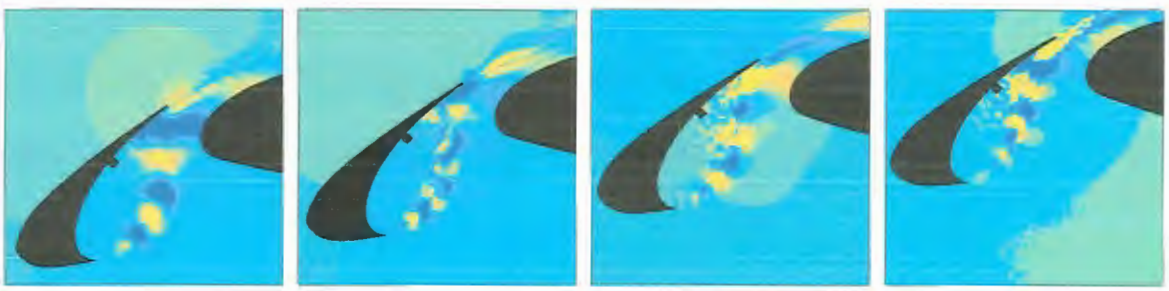

(a) AoA 3° (b) AoA 5° (c) AoA 7° (d) AoA 9°

Figure 44: Real part of second POD mode of first peak in far-field noise spectra sealed cases varying angle of attack. Far-field pressure inner product (P_{Pff}). Seal 0.41 h3w3.

5.4 Seal height effect

The last analysis considers the seal height variation fixing the angle of attack at 3° and seal position, 0.41. Figure 45 shows the pressure coefficient compared to experiments provided by Amaral (2015). As expected no significant changes are observed for seal height of 1 *mm*, since the earlier section presented the result for seal height of 3 *mm* and its presence does not showed relevant modification on the airfoil lift.

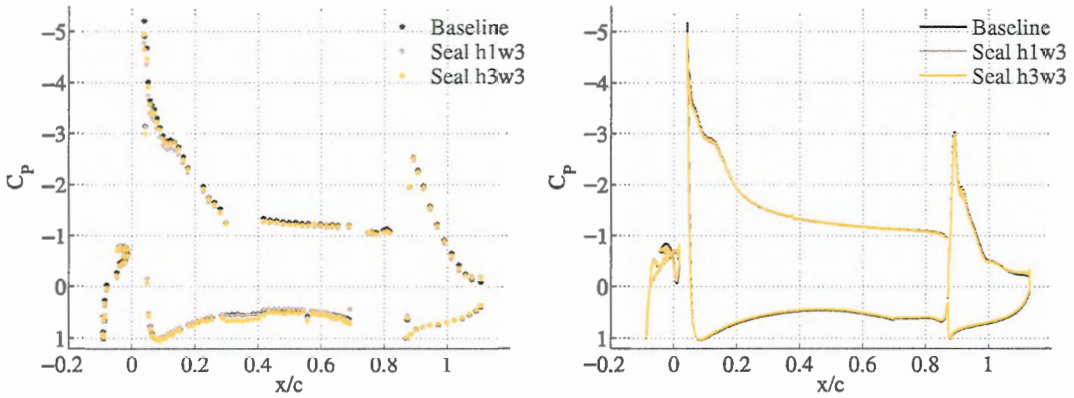

(a) Experimental (AMARAL, 2015)

(b) Numerical

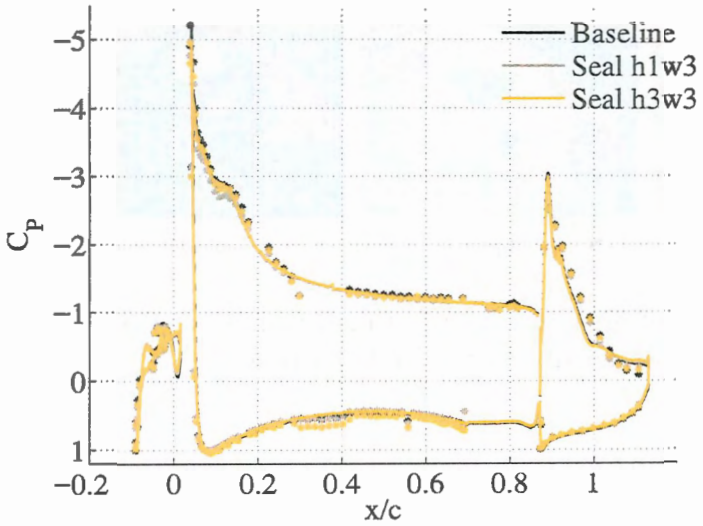

(c) Comparison

Figure 45: Experimental and Numerical c_P for baseline and sealed cases varying seal height. AoA 3°.

Far-field noise spectra is displayed in Fig. 46 and 47. The most interesting result of far-field case for seal height 1 *mm*, is the similarity to the case with seal height three times higher. Then, a small excrescence on the slat cove interferes drastically the slat noise. Also for this smaller seal geometry, the intensity of tonal peaks are not well reproduced by simulations.

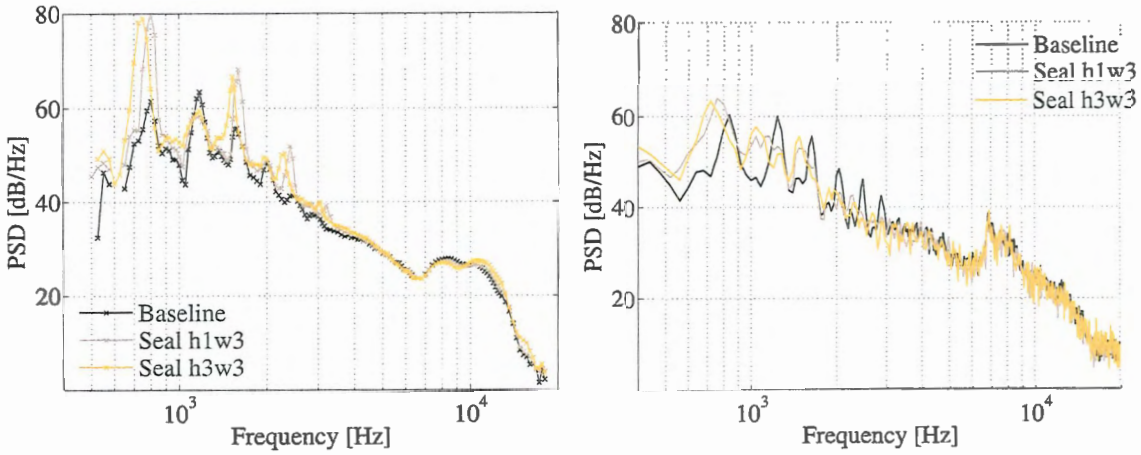

(a) Experimental. (b) Numerical

Figure 46: Experimental (AMARAL, 2015) and Numerical far-field noise spectra presented for baseline and scaled geometries varying its height. $AoA = 3°$

The mean flow analysis shows the same result observed and the sealed geometries present the same behaviour of creating the secondary recirculating region. The main difference is the shape of this bubbles and the distribution of TKE inside cove which is higher for the smaller seal, once the its barrier effect is decreased.

Streamwise velocity fluctuation is presented in Fig. 49 and 50. Results shows clearly that fluctuations have the same behaviour independently the seal height as observed in far-field and mean flow results.

Finally, the POD of cases varying the seal height confirms the earlier results. The frequencies of the peaks are displayed in Fig. 51 for each case. The POD eingevalues are present in Fig. 53 showing that most relevant mode is the first one. The real part of POD mode is presented in Fig. 54. The POD shows same behaviour for both seal heights.

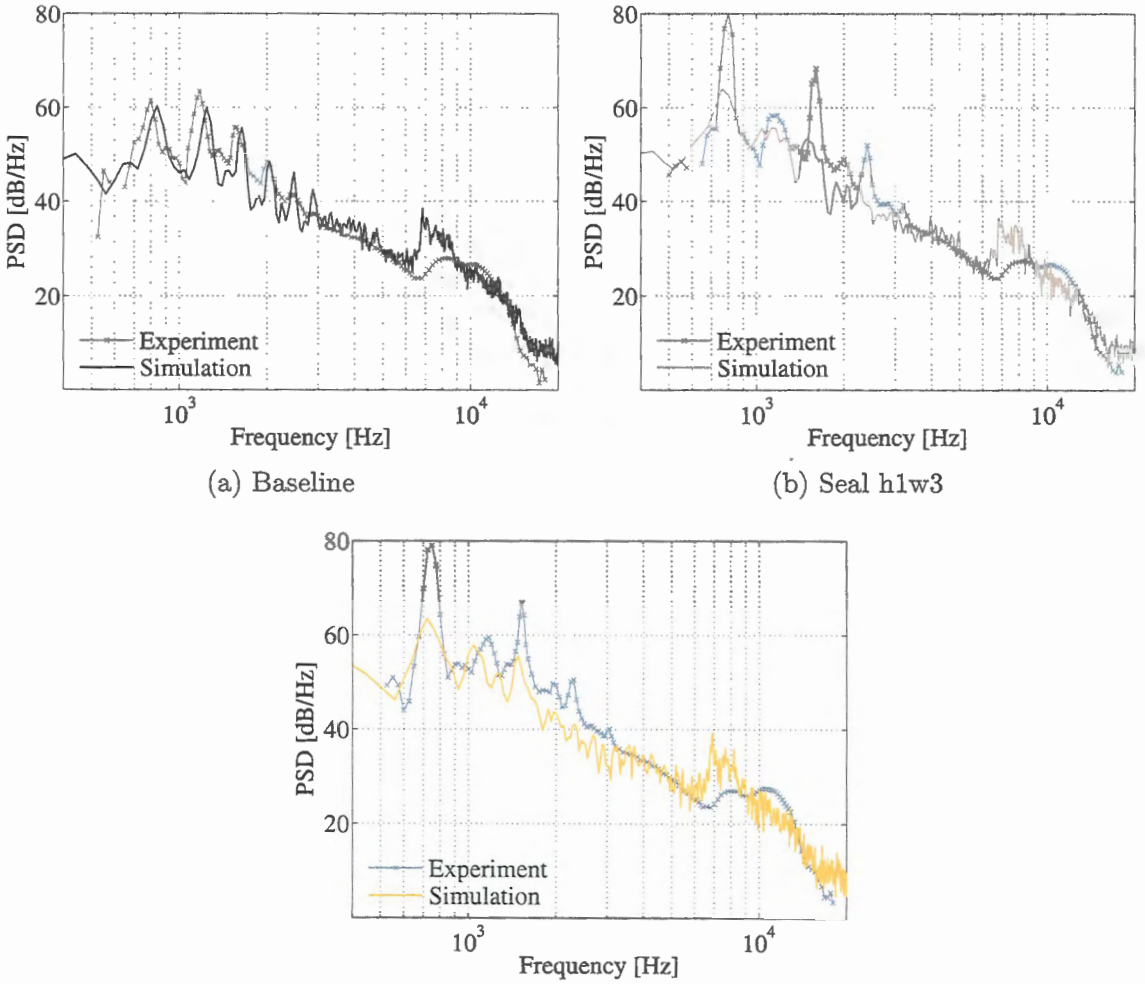

(a) Baseline

(b) Seal h1w3

(c) Seal h3w3

Figure 47: Comparison of Experimental (AMARAL, 2015) and Numerical far-field noise spectra for baseline and sealed geometries varying seal height. $AoA = 3°$

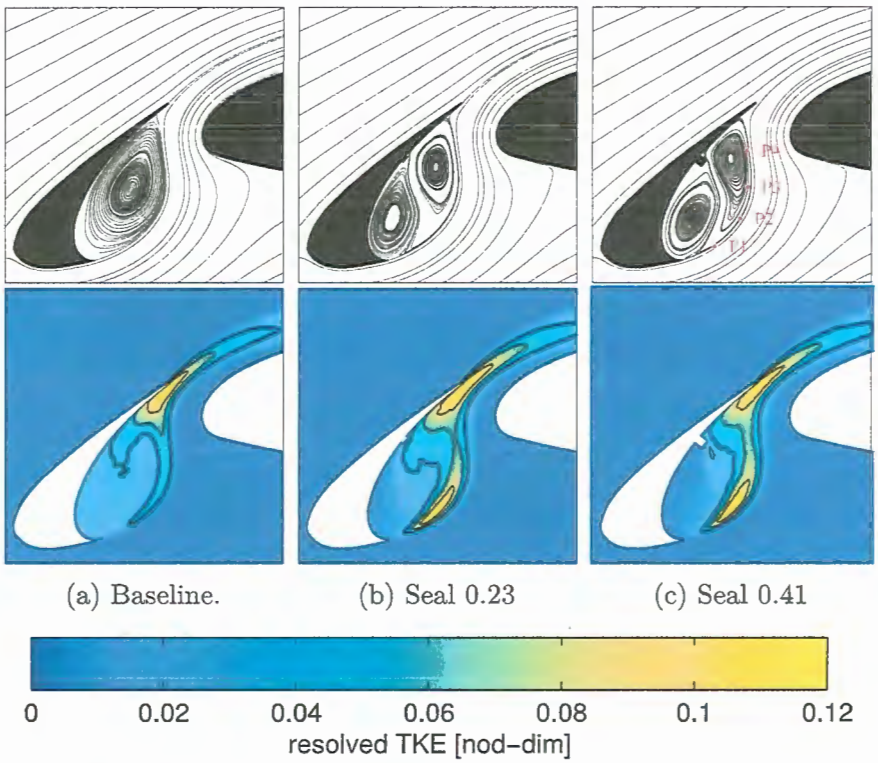

(a) Baseline. (b) Seal 0.23 (c) Seal 0.41

Figure 48: Streamlines and resolved TKE for clean and seal cases varying its height. $AoA = 3°$.

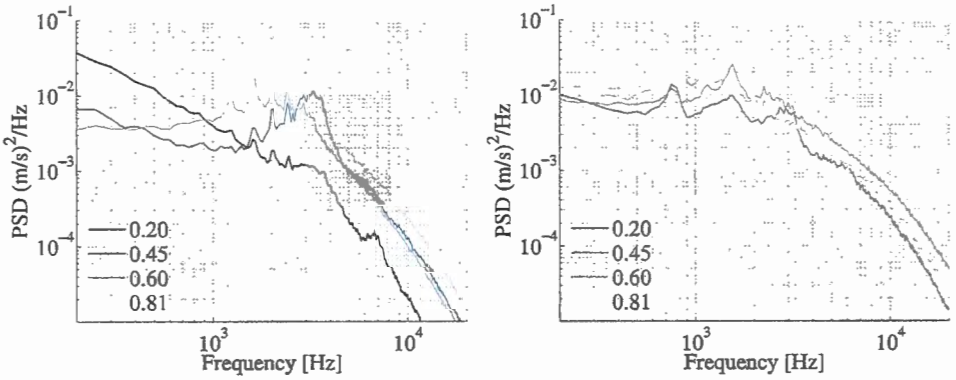

(a) Baseline (b) Seal h1w3

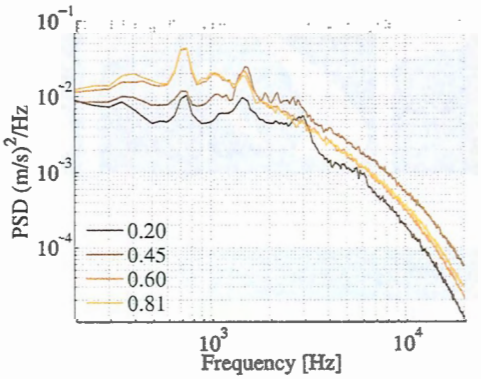

(c) Seal h3w3

Figure 49: Streamwise fluctuation velocity along mixing layer comparing cases evolution. $AoA = 3°$.

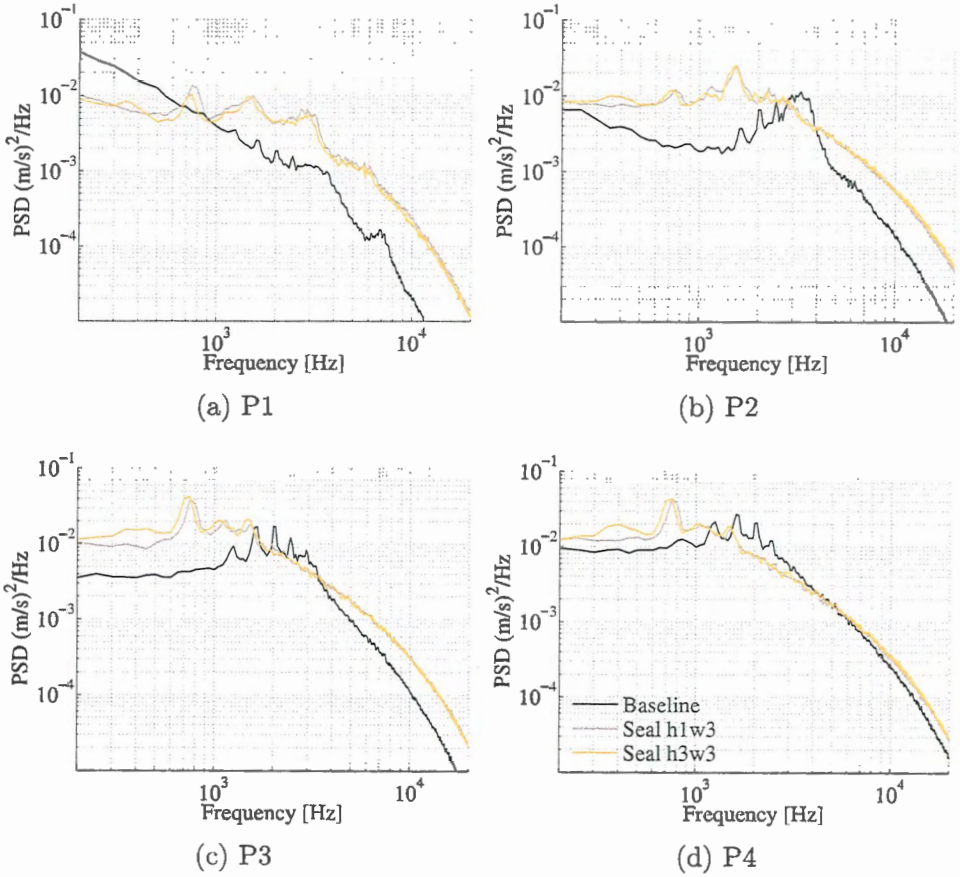

(a) P1 (b) P2

(c) P3 (d) P4

Figure 50: Streamwise fluctuation velocity along mixing layer for each case for each point in mixing layer. $AoA = 3°$.

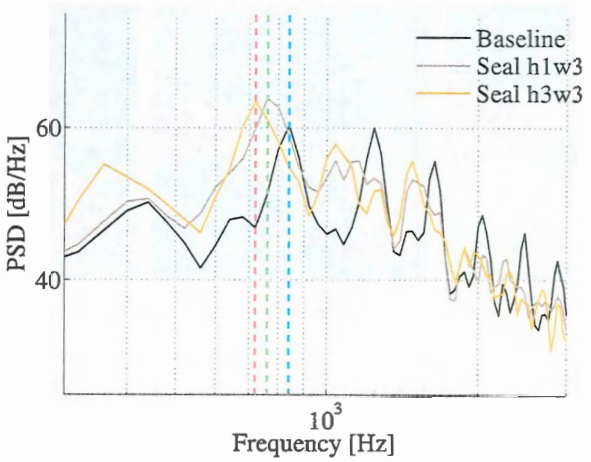

Figure 51: Far-field noise spectra showing the most intense peaks of baseline and sealed configurations. Red line correspond to frequency $f = 720\ Hz$. Green line, $f = 760\ Hz$. Blue line to frequencies $f = 840\ Hz$. $AoA = 3°$.

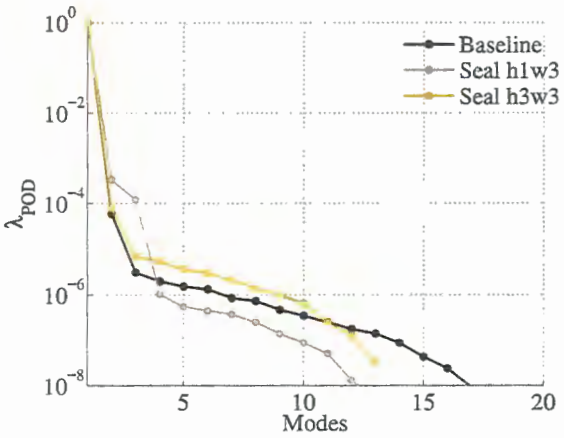

Figure 52: First POD mode

Figure 53: Normalized eigenvalues of POD using far-field pressure inner product (P_{Pff}) in the frequency of the most intense peak of baseline and sealed configurations varying its height (See Fig. 51). $AoA = 3°$, seal 0.41.

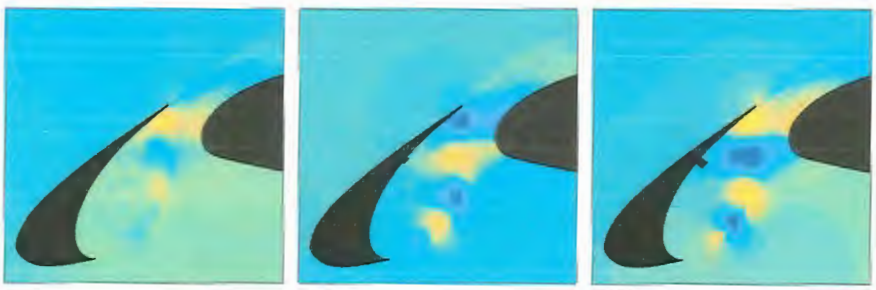

(a) Baseline (b) Seal h1w3 (c) Seal h3w3

Figure 54: Real part of first POD mode of first peak in far-field noise spectra for baseline and sealed cases varying its height. Far-field pressure inner product (P_{Pff}). $AoA = 3°$, seal 0.41.

5.5 LST applied in cases without seal

Since the Linear Stability Theory was not useful to analyse the sealed cases, this theory was applied in simulations data of cases without seal provided by Souza (2016). The cited work analysed the influence of deflection and angle of attack variations of a clean slat geometry. The main ideia here was to observe the evolution of the mixing layer most unstable modes with the fluctuation amplitude provided by LST and the propagated noise obtained by these cases.

The simulations were performed with the same flow parameters of section 5.1. Geometrical parameters and nomenclature are presented in the list below:

Table 3: Nomeclature and geometrical parameters of slat in percentage of c_{stowed} (gap and slat deflection was fixed to 2.95% of c_{stowed} and 30°, respectivelly). Cases simulated by Souza (2016).

	AoA	Overlap
olAa4	4°	−2.50 %
olAa8	8°	−2.50 %
olBa4	4°	−2.95 %
olCa4	4°	1.00 %

Figure 55 compares the mixing layer path of cases listed above. The baseline slat geometry (case olAa4) is presented in black. As expected the angle of attack increasing shrinks the recirculation bubble and the same effect is observed for positive overlap while more negative overlap extends the mixing layer and approximates the reattachment point towards the trailing edge. The farfield noise spectra of these cases is presented in the study of Souza (2016), showing that noise level decreases in the sequence olBa4, olAa4, olAa8 and olCa4, respectivelly.

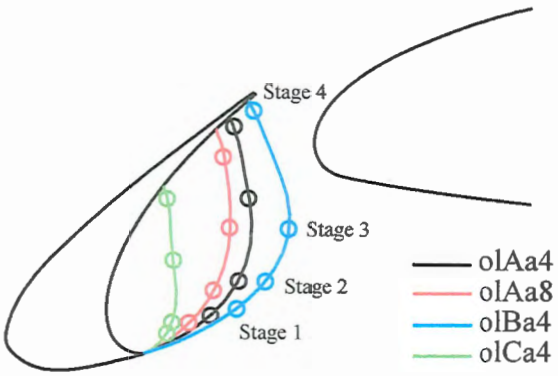

Figure 55: Scheme showing the stages of the mixing layer path of cases without seal. Extracted from Souza (2016) and modified.

Evolution of mixing layer velocity profile is presented in Fig. 56 for all cases. The tanh function approximates well the mixing layer velocity profile and the LST was used to investigate the behaviour of most unstable modes.

The initial question of this particular study was observe if the tonal peaks of farfield noise were related to the most unstable modes. Figure 57 shows the fluctuations amplitude calculated along the mixing layer appling the LST. The evolution of amplitude is quite similar to that found in fluctuation velocity spectra of these cases presented in Fig. 58, reproduced here from Souza (2016) for comparison. This result indicates that tonal peaks are not related directly to the behaviour of the mixing layer most unstable modes because the peaks are not present in spectra obtained by LST. Another aspect to observe is that if the peaks were related to these unstable modes it was expected that the noisier case (olBa4) would present the higher amplitude spectra than all cases and for quieter one (olCa4), the lesser amplitude, but this feature is not observed from LST results.

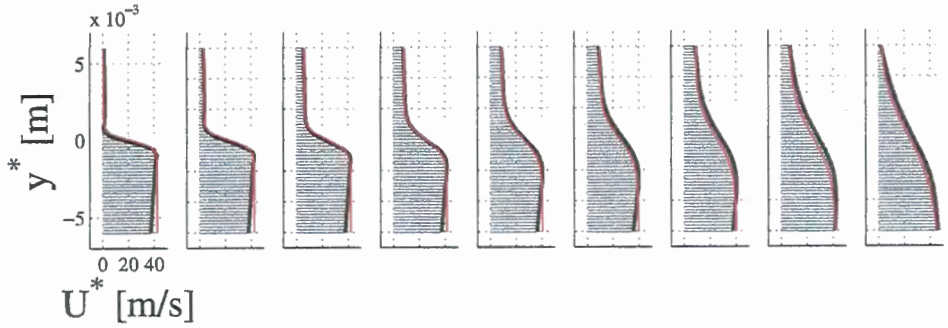

(a) olAa4

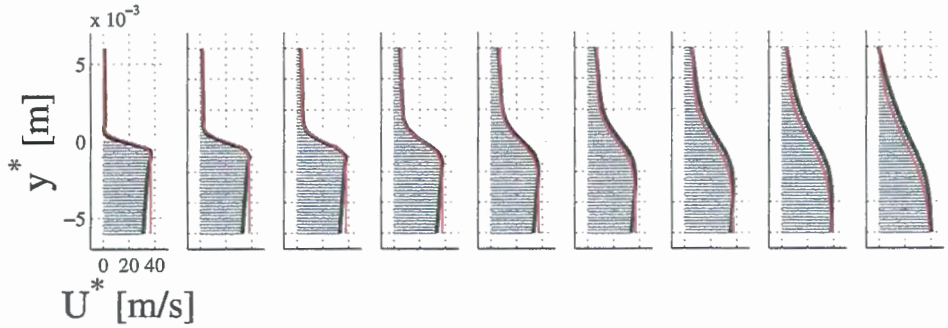

(b) olAa8

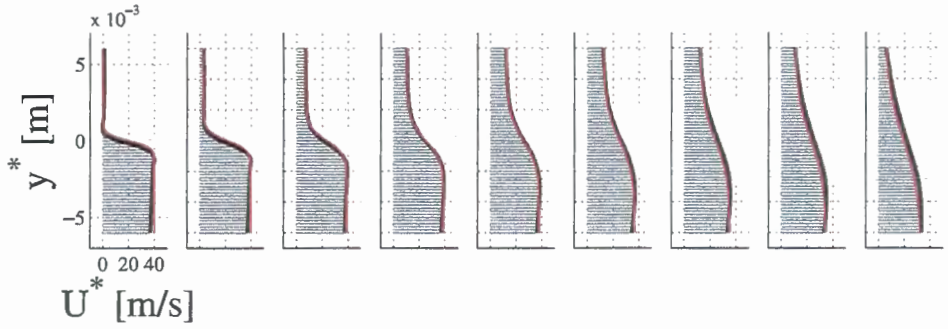

(c) olBa4

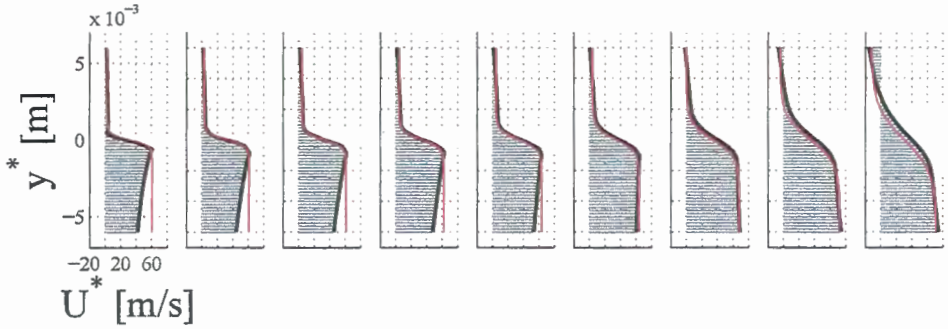

(d) olCa4

Figure 56: Mixing layer velocity profile of the cases without seal. Black stroke represent the velocity extracted from simulation and red stroke the tanh fitting for LST calculation. The gray region represent the vorticity thickness. Simulation data was provided by Souza (2016).

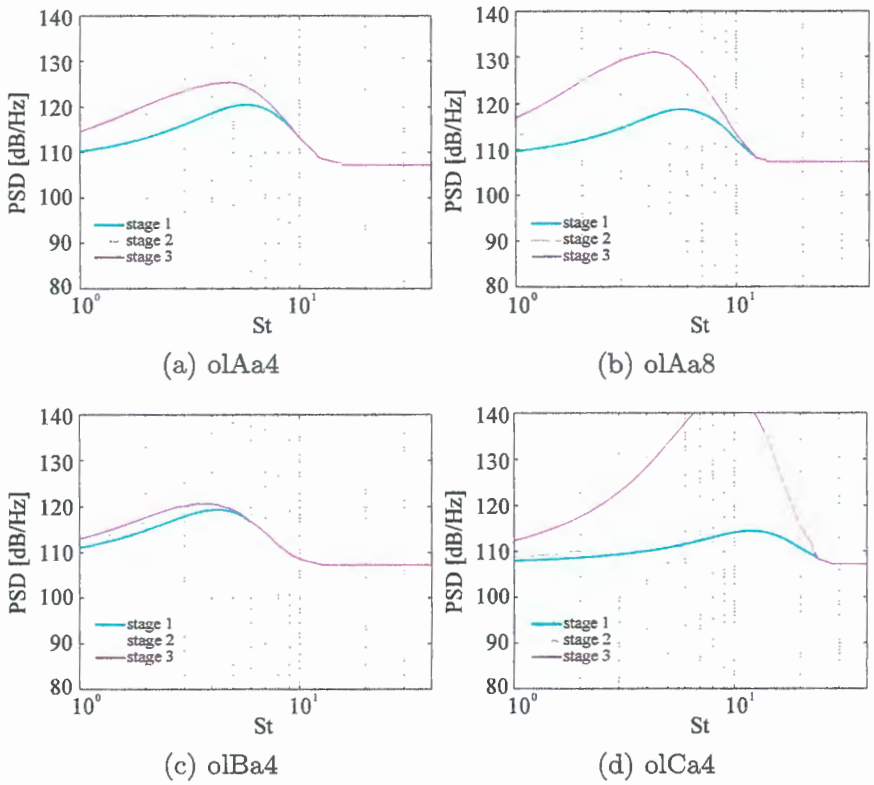

(a) olAa4 (b) olAa8

(c) olBa4 (d) olCa4

Figure 57: Fluctuation amplitude of cases without seal considering the LST calculation.

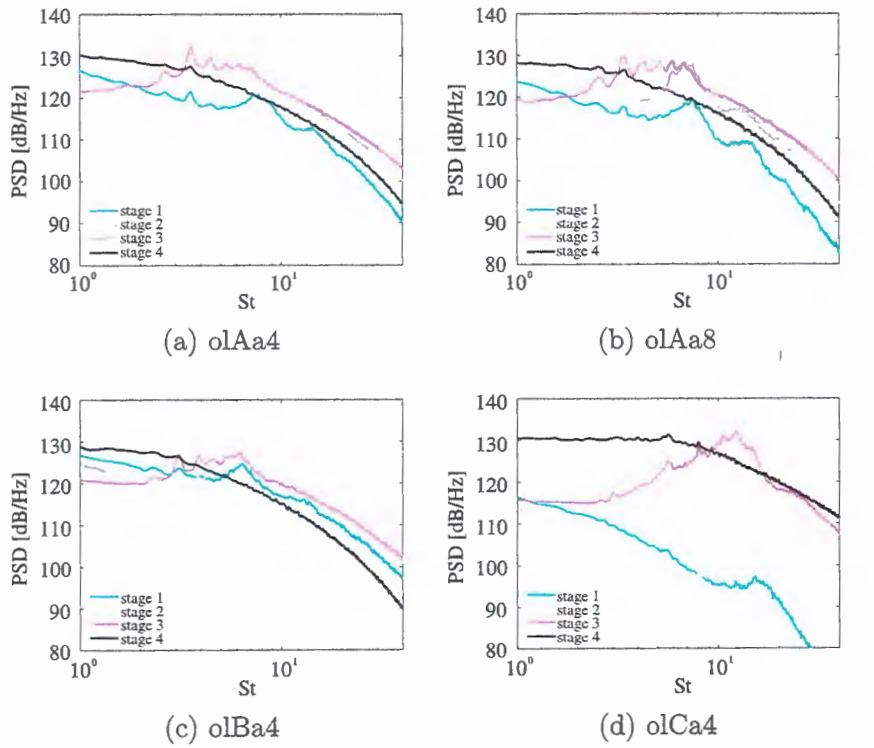

(a) olAa4 (b) olAa8

(c) olBa4 (d) olCa4

Figure 58: Mixing layer fluctuation velocity of the cases without seal (SOUZA, 2016).

6 CONCLUSION

The far-field noise spectra shows the inclusion of the seal drastically changes the slat propagated noise with no significatives effects on the airfoil lift. This effect can be observed even for the smallest height, 1 mm. Experimental results show well-defined peaks in the noise spectrum that PowerFLOW could not reproduce for the noisiest configurations (seal positions 0.41 and 0.60). The frequency of the tonal peaks, however, agreed reasonably well. Several efforts were made to understand this inability in reach this tonal intensity. In the preliminary studies section is presented the simulation independency tests proving that simulations converged. Then, we assume that code were not able to solve the fully phenomena to achieve the tonal peaks intensity. Some possible explanation of this inability could be the turbulence model implemented that may dissipate the structures convected between the recirculations for sealed cases that presents two bubbles (more complex recirculating dynamics). This is plausible since the refinement did not present better results. Despite of that, the analysis of the flow characteristiscs were carried out to understand the main differences observed in the noisier cases.

The study of seal position variation on the slat cove, shows that for some positions of seal (0.41 and 0.60, the noisiest ones) a secondary counter-rotating bubble emmerges inside recirculation region. The bubbles presence affects the mean flow and TKE shows an additional energetic region in the mixing layer that is closer to the cusp and the energetic region near the reattachment point that is observed in all cases. The presence of this bubble also creates a region from which the turbulence is directly convected to mixing layer creating a more complex phenomena.

Angle of attack variation study also indicated the presence of secondary peaks near the tonal peaks observed in experiments. This behaviour were not clearly found in experimental spectra and this might due the higher intensity of tonal peaks that could overcome the "sub-peaks".

The spectra of the streamwise velocity fluctuations development also identifies the drastic difference between the cases with only one bubble compared to the two bubbles ones. When only one bubble is present, the fluctuations in the mixing layer develop from the high frequency band to lower frequencies and peaks, that could be related to far-field noise tonals, emmerge before the reattachment. For the two bubbles cases which are noisier, the fluctuations are higher since earlier stages of mixing layer, showing clearer peaks. The barrier effect evidenced for sealed configurations are also present in the fluctuation spectra and it is more clearly visualized for seal 0.23 compared to baseline. For noisier cases this barrier effect are not observed since the presence of the secondary bubbles directly convects the structures to mixing layer by the path created between the bubbles.

POD was applied to study the behaviour of the coherent structures present in the slat flow dynamics with seal presence. For this study the inner product used highlighted the structures that were related to the pressure in far-field in order to observe the effect that are propagated to the listener and not only confined to the near-field. The results show that for cases which streamlines show one bubble, the structures are more defined at latter stages of the mixing layer while for two bubbles configurations, this structures emmerged earlier and were more energetic. Following the literature we can also identify the two most intense peaks of noise spectra as the second and third Rossiter modes and the fundamental mode were not observed.

LST were also applied to study the evolution of the most unstable spatial modes that occurs in mixing layer and observe their relationship with the tonal peaks. Results show that this theory presents the spatial amplification of the broadband fluctuations of streamwise velocity, is very similar to that observed in simulations for cases with one bubble. For noisier two bubbles cases, however, it was not observed and the simulation results showed different pattern of the fluctuation than that calculated by theory. The tonal peaks was not present in the theorical results, so LST could not be used to determine its frequency or intensity. Then, this result is another indicative that tonal peaks are related to the Rossiter acoustic feedback mechanism. The main contribution of LST was the measure of the vorticty thickness which showed that two bubble cases present thicker mixing layers.

7 FUTURE WORKS

For future works it is indicated to investigate the presence of sub-peaks that appear in the tonal peaks neighborhood observed in the far-field noise spectra. This phenomena could be related to the preference of some Rossiter modes and could explain, for example, the seal at position 0.60 which experiments showed the second most intense peak lower than third one and this may be related to some mixing layer change that makes the Rossiter modes migrate to the next mode along the mixing layer creating a cycle that are closed in a integer number. The investigation using tridimensional POD is also encouraged in order to study this effect and understanding the code inability to reproduce the tonal peaks intensity.

The analysis of the recirculating structures are also indicated for future works to observe the effect of the bulb seal in the strucutres convected to the mixing layer for the configurations that show two bubbles inside slat cove.

BIBLIOGRAPHY

AMARAL, F. R. et al. Experimental study of the effect of a small 2d excrescence placed on the slat cove surface of an airfoil on its acoustic noise. In: **21st AIAA/CEAS Aeroacoustics Conference**. [S.l.: s.n.], 2015. p. 3138.

AMARAL, F. R. d. **Efeito Aeroacústico de Excrescências Bidimensionais na Cova de um Eslate**. 2015. Dissertação (Mestrado) — Escola de Engenharia de São Carlos - USP, 2015.

BERKOOZ, G.; HOLMES, P.; LUMLEY, J. L. The proper orthogonal decomposition in the analysis of turbulent flows. **Annual review of fluid mechanics**, Annual Reviews 4139 El Camino Way, PO Box 10139, Palo Alto, CA 94303-0139, USA, v. 25, n. 1, p. 539–575, 1993.

BHATNAGAR, P. L.; GROSS, E. P.; KROOK, M. A model for collision processes in gases. i. small amplitude processes in charged and neutral one-component systems. **Physical review**, APS, v. 94, n. 3, p. 511, 1954.

BOLTZMANN, L. Weitere studien über das wärmegleichgewicht unter gasmolekülen. In: **Kinetische Theorie II**. [S.l.]: Springer, 1970. p. 115–225.

BRES, G. A.; PÉROT, F.; FREED, D. Properties of the lattice-boltzmann method for acoustics. In: **Proc. AIAA Aeroacoustics Conf., Miami, USA**. [S.l.: s.n.], 2009.

CHEN, S.; DOOLEN, G. D. Lattice boltzmann method for fluid flows. **Annual review of fluid mechanics**, Annual Reviews 4139 El Camino Way, PO Box 10139, Palo Alto, CA 94303-0139, USA, v. 30, n. 1, p. 329–364, 1998.

CHOUDHARI, M. et al. Slat cove noise modeling: A posteriori analysis of unsteady rans simulations. **AIAA paper**, v. 2468, p. 2002, 2002.

CHOUDHARI, M. M.; KHORRAMI, M. R. Effect of three-dimensional shear-layer structures on slat cove unsteadiness. **AIAA journal**, v. 45, n. 9, p. 2174–2186, 2007.

COLONIUS, T.; FREUND, J. Pod analysis of sound generation by a turbulent jet. In: **40th AIAA Aerospace Sciences Meeting & Exhibit**. [S.l.: s.n.], 2002. p. 72.

CRIGHTON, D. G. Airframe noise. In: **Aeroacoustics of flight vehicles: theory and practice. Volume 1: noise sources**. [S.l.: s.n.], 1991. v. 1, p. 391–447.

DECK, S.; LARAUFIE, R. Numerical investigation of the flow dynamics past a three-element aerofoil. **Journal of Fluid Mechanics**, Cambridge Univ Press, v. 732, p. 401–444, 2013.

DOBRZYNSKI, W. Almost 40 years of airframe noise research: what did we achieve? **Journal of aircraft**, v. 47, n. 2, p. 353–367, 2010.

DOBRZYNSKI, W. et al. Airframe noise studies on wings with deployed high-lift devices. In: **4th AIAA/CEAS Aeroacoustics Conference**. [S.l.: s.n.], 1998. p. 2337.

DOBRZYNSKI, W.; POTT-POLENSKE, M. Slat noise source studies for far-field noise prediction. **AIAA/CEAS Aeroacoustics Conference. Maastricht, Holanda**, [s.n.], 2001.

EXA, C. **PowerFLOW - Release 4.4 User's Guide**. [S.l.], 2012.

FARASSAT, F. Linear acoustic formulas for calculation of rotating blade noise. **AIAA journal**, v. 19, n. 9, p. 1122–1130, 1981.

FARASSAT, F.; SUCCI, G. P. A review of propeller discrete frequency noise prediction technology with emphasis on two current methods for time domain calculations. **Journal of Sound and Vibration**, Elsevier, v. 71, n. 3, p. 399–419, 1980.

FINK, M. R.; SCHLINKE, R. H. Airframe noise component interaction studies. **Journal of Aircraft**, v. 17, n. 2, p. 99–105, 1980.

HAYES, J. et al. Airframe noise characteristics of a 4.7 percent scale dc-10 model. In: **3rd AIAA/CEAS Aeroacoustics Conference**. [S.l.: s.n.], 1997. p. 1594.

HE, X.; LUO, L.-S. Theory of the lattice boltzmann method: From the boltzmann equation to the lattice boltzmann equation. **Physical Review E**, APS, v. 56, n. 6, p. 6811, 1997.

HUERRE, P.; MONKEWITZ, P. A. Local and global instabilities in spatially developing flows. **Annual review of fluid mechanics**, Annual Reviews 4139 El Camino Way, PO Box 10139, Palo Alto, CA 94303-0139, USA, v. 22, n. 1, p. 473–537, 1990.

IMAMURA, T. et al. A far-field noise and near-field unsteadiness of a simplified high-lift-configuration model (slat). In: **47th AIAA Aerospace Sciences Meeting Including The New Horizons Forum and Aerospace Exposition**. [S.l.: s.n.], 2009. p. 1239.

JENKINS, L. N.; KHORRAMI, M. R.; CHOUDHARI, M. Characterization of unsteady flow structures near leading-edge slat: Part i. piv measurements. **AIAA paper**, v. 2801, p. 2004, 2004.

JUNIPER, M. P.; HANIFI, A.; THEOFILIS, V. Modal stability theorylecture notes from the flow-nordita summer school on advanced instability methods for complex flows, stockholm, sweden, 2013. **Applied Mechanics Reviews**, American Society of Mechanical Engineers, v. 66, n. 2, p. 024804, 2014.

KHORRAMI, M. R.; BERKMAN, M. E.; CHOUDHARI, M. Unsteady flow computations of a slat with a blunt trailing edge. **AIAA journal**, v. 38, n. 11, p. 2050–2058, 2000.

KHORRAMI, M. R.; LOCKARD, D. P. Effects of geometric details on slat noise generation and propagation. **International Journal of aeroacoustics**, Multi-Science, v. 9, n. 4, p. 655–678, 2010.

KHORRAMI, M. R.; SINGER, B. A.; LOCKARD, D. P. Time-accurate simulations and acoustic analysis of slat free-shear-layer: Part ii. **AIAA paper**, v. 2002-2579, 2002.

KOLB, A. et al. Aeroacoustic wind tunnel measurements on a 2d high-lift configuration. **AIAA paper**, v. 3447, p. 2007, 2007.

_____. Aeroacoustic wind tunnel measurements on a 2d high-lift configuration. **AIAA paper**, v. 3447, p. 2007, 2007.

LIGHTHILL, M. On sound gcncratcd acrodynamically. i. **General Theory. Proc. Roy. Soc., ser. A**, v. 211, p. 564–587, 1952.

LOCKARD, D. P. An efficient, two-dimensional implementation of the ffowcs williams and hawkings equation. **Journal of Sound and Vibration**, Elsevier, v. 229, n. 4, p. 897–911, 2000.

LOCKARD, D. P.; CHOUDHARI, M. Noise radiation from a leading-edge slat. In: **15th AIAA/CEAS Aeroacoustics Conference (30th AIAA Aeroacoustics Conference)**. [S.l.: s.n.], 2009. p. 3101.

MACARAEG, M. Fundamental investigations of airframe noise. In: **4th AIAA/CEAS Aeroacoustics Conference**. [S.l.: s.n.], 1998. p. 2224.

MANOHA, E. et al. Slat noise measurement and numerical prediction in the valiant programme. In: **18th AIAA/CEAS Aeroacoustics Conference (33rd AIAA Aeroacoustics Conference)**. American Institute of Aeronautics and Astronautics, 2012. p. 2100. Disponível em: <http://dx.doi.org/10.2514/6.2012-2100>.

MONKEWITZ, P. A.; HUERRE, P. Influence of the velocity ratio on the spatial instability of mixing layers. **The Physics of Fluids**, AIP, v. 25, n. 7, p. 1137–1143, 1982.

_____. Influence of the velocity ratio on the spatial instability of mixing layers. **The Physics of Fluids**, v. 25, n. 7, p. 1137–1143, 1982.

PAGANI JR, C. C.; SOUZA, D. S.; MEDEIROS, M. A. F. Slat noise: Aeroacoustic beamforming in closed-section wind tunnel with numerical comparison. **AIAA Journal**, v. 54, n. 7, p. 2100–2115, 2016. ISSN 0001-1452.

ROGER, M.; PÉRENNÈS, S. Low-frequency noise sources in two-dimensional high-lift devices. In: **6th Aeroacoustics Conference and Exhibit**. [S.l.: s.n.], 2000. p. 1972.

ROWLEY, C. W. **Modeling, simulation, and control of cavity flow oscillations**. 2002. Tese (Doutorado) — California Institute of Technology, 2002.

SATTI, R. et al. Simulation of flow over a 3-element airfoil using a lattice-boltzmann method. In: **46th AIAA Aerospace Sciences Meeting and Exhibit**. [S.l.: s.n.], 2008. p. 549.

SIMõES, L.; SOUZA, D.; MEDEIROS, M. On the small effect of boundary layer thicknesses on slat noise. In: **17th AIAA/CEAS Aeroacoustics Conference (32nd AIAA Aeroacoustics Conference)**. [S.l.: s.n.], 2011. p. 2906.

SIMõES, L. G. C. **Estudo da geração de som em um eslate utilizando código comercial**. 2011. Dissertação (Mestrado) — Escola de Engenharia de São Carlos - USP, 2011.

SIROVICH, L. Turbulence and the dynamics of coherent structures. i-iii. **Quarterly of applied mathematics**, v. 45, n. 3, 1987.

SOUZA, D. et al. Effect of an excrescence in the slat cove: Flow-field, acoustic radiation and coherent structures. **Aerospace Science and Technology**, Elsevier, 2015.

SOUZA, D. S. **Simulação numérica de ruído de eslate em configurações práticas usando um código comercial**. 2012. Dissertação (Mestrado) — Escola de Engenharia de São Carlos - USP, 2012.

SOUZA, D. S. **Numerical study of the large scale turbulent structures responsible for slat noise generation**. 2016. Tese (Doutorado) — University of São Paulo, 2016.

SOUZA, D. S.; RODRIGUEZ, D.; MEDEIROS, M. A. F. A study of the sources of slat noise using proper orthogonal decomposition. In: **19th AIAA/CEAS Aeroacoustics Conference**. [S.l.: s.n.], 2013. p. 2163.

STORMS, B. et al. Aeroacoustic measurements of slat noise on a three-dimensional high-lift system. In: **5th AIAA/CEAS Aeroacoustics Conference and Exhibit**. [S.l.: s.n.], 1999. p. 1957.

STREETT, C. Numerical simulation of fluctuations leading to noise in a flap-edge flowfield. In: **36th AIAA Aerospace Sciences Meeting and Exhibit**. [S.l.: s.n.], 1998. p. 628.

TAKEDA, K. et al. Unsteady aerodynamics of slat cove flow in a high-lift device configuration. In: **39th Aerospace Sciences Meeting and Exhibit**. [S.l.: s.n.], 2001. p. 706.

WILLIAMS, J. F.; HAWKINGS, D. L. Sound generation by turbulence and surfaces in arbitrary motion. **Philosophical Transactions of the Royal Society of London. Series A, Mathematical and Physical Sciences**, The Royal Society, v. 264, n. 1151, p. 321–342, 1969.

YAKHOT, V.; ORSZAG, S. A. Renormalization group analysis of turbulence. i. basic theory. **Journal of scientific computing**, Springer, v. 1, n. 1, p. 3–51, 1986.

ZOU, Q.; HE, X. On pressure and velocity boundary conditions for the lattice boltzmann bgk model. **Physics of fluids**, AIP, v. 9, n. 6, p. 1591–1598, 1997.